JOURNAL OF GEOPHYSICAL RESEARCH: SOLID EARTH, VOL. 118, 3785–3808, doi:10.1002/jgrb.50261, 2013

Laterally propagating slow slip events in a rate and state friction model with a velocity-weakening to velocity-strengthening transition

J. C. Hawthorne[1,2] and A. M. Rubin[1]

Received 21 August 2012; revised 31 May 2013; accepted 20 June 2013; published 24 July 2013.

[1] We investigate the behavior of simulated slow slip events using a rate and state friction model that is steady state velocity weakening at low slip speeds but velocity strengthening at high slip speeds. Our simulations are on a one-dimensional (line) fault, but we modify the elastic interactions to mimic the elongate geometry frequently observed in slow slip events. Simulations exhibit a number of small events as well as periodic large events. The large events propagate approximately steadily "along strike," and stress and slip rate decay gradually behind the propagating front. Their recurrence intervals can be determined by considering what is essentially an energy balance requirement for long-distance propagation. It is possible to choose the model parameters such that the simulated events have the stress drops, slip velocities, and propagation rates observed in Cascadia.

Citation: Hawthorne, J. C., and A. M. Rubin (2013), Laterally propagating slow slip events in a rate and state friction model with a velocity-weakening to velocity-strengthening transition, *J. Geophys. Res. Solid Earth*, *118*, 3785–3808, doi:10.1002/jgrb.50261.

1. Introduction

[2] Slow slip events have been observed at a number of plate boundaries over the past 10 years. They usually occur on the plate interface near the transition from the locked zone to the steadily sliding region. In observed events, the slow slip region slides at rates between 10 and 100 times the plate convergence rate for a few days to a few months, accumulating a few centimeters of displacement. In parts of some subduction zones, slow slip events occur periodically, with recurrence intervals between a few months and several years. In many of these periodic events, the along-strike extent of the slow slip region is longer than its along-dip extent and the slipping region propagates along strike at rates of order 10 km/day during each event [e.g., *Dragert et al.*, 2001; *Obara*, 2002; *Schwartz and Rokosky*, 2007; *Peng and Gomberg*, 2010]. In this paper, we consider how and whether one proposed frictional sliding model can reproduce these observations.

[3] Several constitutive laws have been proposed to govern the frictional strength of the sliding surface in the slow slip region. Within the rate and state friction framework, episodic slow slip events have been produced on (1) faults within a restricted size range governed by "standard" velocity-weakening friction [*Yoshida and Kato*, 2003; *Liu and Rice*, 2005, 2007; *Rubin*, 2008; *Mitsui and Hirahara*, 2008; *Ariyoshi et al.*, 2009; *Liu and Rice*, 2009; *Skarbek et al.*, 2012], (2) faults that dilate and exhibit reduced pore pressure as the slip speed increases [*Segall and Rice*, 1995; *Suzuki and Yamashita*, 2009; *Liu and Rubin*, 2010; *Segall et al.*, 2010; *Yamashita and Suzuki*, 2011], and (3) faults governed by a friction law that is steady state velocity weakening at low slip speeds but velocity strengthening at high slip speeds [*Okubo and Dietrich*, 1986; *Weeks*, 1993; *Shibazaki and Iio*, 2003; *Shibazaki and Shimamoto*, 2007; *Beeler*, 2009; *Matsuzawa et al.*, 2010; *Shibazaki et al.*, 2010; *Bar Sinai et al.*, 2012].

[4] Here we explore the third variant: that a friction law with a velocity-weakening to velocity-strengthening transition is relevant for the part of the plate interface between the locked and steadily sliding regions. Such a friction law is consistent with one common physical interpretation of rate and state friction [e.g., *Brechet and Estrin*, 1994; *Estrin and Brechet*, 1996; *Rice et al.*, 2001; *Nakatani and Scholz*, 2006; *Beeler*, 2009], but it is not obvious from that physical model that the conditions of the downdip transition zone should favor a weakening to strengthening friction law more than other regions do. In the laboratory, a friction law with a weakening to strengthening transition is suggested by experiments on a variety of materials [e.g., *Dieterich*, 1972; *Shimamoto*, 1986; *Kilgore et al.*, 1993; *Weeks*, 1993; *Reinen et al.*, 1994; *Moore et al.*, 1997], though it has not been observed in the few experiments performed on rock types and with pressure and temperature conditions plausibly appropriate for slow slip [e.g., *He et al.*, 2006, 2007; *Boettcher et al.*, 2007].

[5] In this study, we seek a quantitative understanding of a number of features of slow slip events simulated with a velocity-weakening to velocity-strengthening law. In particular, we will consider what controls the slip rate, propagation rate, and recurrence interval of the simulated

[1]Department of Geosciences, Princeton University, Princeton, New Jersey, USA.
[2]Now at Division of Geological and Planetary Sciences, California Institute of Technology, Pasadena, California, USA.

Corresponding author: J. C. Hawthorne, Division of Geological and Planetary Sciences, California Institute of Technology, 1200 E. California Blvd., MS 252-21, Pasadena, CA 91125, USA. (jessicah@caltech.edu)

2169-9313/13/10.1002/jgrb.50261

events. However, matching just these few properties of the observed events is not enough to determine whether this friction law is appropriate for slow slip. If sufficient tuning of the relevant parameters is allowed, any of the three classes of models described above is capable of reproducing these general features. Therefore, a second goal of this paper is to understand the modeled events well enough to provide a framework for understanding additional properties of slow slip events. We use some of the results presented here in a companion paper [*Hawthorne and Rubin*, 2013], where we assess whether our model can reproduce the observed tidal modulation of slip and the propagation velocity of back-propagating fronts.

[6] We begin in section 2 by introducing our chosen friction law and model geometry. We describe some properties of the velocity and stress profiles of the slow slip events in section 3. In section 4, we describe the behavior of the fault in the inter-slow slip period and discuss event nucleation. We determine what controls the recurrence interval and slip rates of events that propagate long distances in section 5. Finally, in section 6, we compare the features we have modeled to observations of tremor and slow slip in Cascadia.

2. Model Setup

2.1. Friction Law

[7] The frictional strength τ of our modeled fault is given by one form of the rate and state friction equations [e.g., *Dieterich*, 2007]:

$$\tau(V,\theta) = f^*\sigma + a\sigma \log\left(\frac{V}{V^*}\right) + b\sigma \log\left(\frac{V_c\theta}{D_c} + 1\right). \quad (1)$$

Here the local slip rate V and the local state θ change with time. State can be thought of as a measure of the strength of microscopic asperity contacts. σ is the effective normal stress, and a and b are nondimensional constants. a determines the amplitude of the "direct" effect: how stress varies due to changes in velocity at constant state. b determines the amplitude of the evolution effect: how stress varies due to changes in state at constant velocity. D_c is a length scale that controls the slip distance required for state evolution. f^* is a reference coefficient of friction, and V^* is a reference velocity.

[8] To fully describe the frictional strength, equation (1) must be coupled with an evolution law for how state changes with time. We have run simulations with both the "aging" law

$$\frac{d\theta}{dt} = 1 - \frac{V\theta}{D_c} \quad (2)$$

and the "slip" law

$$\frac{d\theta}{dt} = -\frac{V\theta}{D_c} \ln\left(\frac{V\theta}{D_c}\right) \quad (3)$$

[e.g., *Ruina*, 1983; *Marone*, 1998].

[9] Both the aging and slip laws are such that for a fault slipping at a constant rate V, state evolves toward a steady state value of D_c/V. The steady state frictional strength is then given by inserting $\theta = D_c/V$ into equation (1):

$$\tau_{ss}(V) = f^*\sigma + a\sigma \log\left(\frac{V}{V^*}\right) + b\sigma \log\left(\frac{V_c}{V} + 1\right). \quad (4)$$

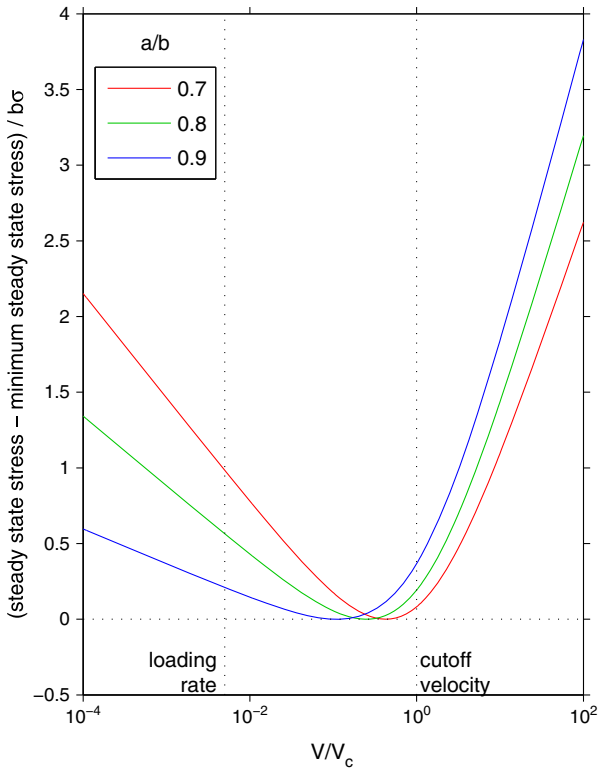

Figure 1. Steady state frictional strength τ_{ss} minus the minimum steady state strength $\tau_{ss\text{-}min}$ as a function of slip rate for several values of a/b. The fault is steady state velocity weakening at slip speeds smaller than $V_{\tau\text{-}min} = V_c(b-a)/a$ and steady state velocity strengthening at higher slip speeds.

In this equation, if the slip rate V increases, the direct effect term $a\sigma \log(V/V^*)$ increases, but the evolution effect term $b\sigma \log(V_c/V + 1)$ decreases. At low slip speeds ($V \ll V_c$), this leads to a frictional strength that decreases with increasing slip rate if $b > a$. $d\tau_{ss}/d\log(V)$ tends to $-(b-a)\sigma$ at low speeds, as is the case for standard rate and state friction. However, equations (1) and (4) include a cutoff on the influence of state on stress, implemented with the "+1" in the evolution effect term. Once state is smaller than about D_c/V_c, further decreases in state have diminishing contributions to changes in frictional strength. At high slip speeds, the fault is then steady state velocity strengthening regardless of the value of b, and $d\tau_{ss}/d\log(V)$ tends to $a\sigma$.

[10] These behaviors can be seen in Figure 1, where we plot the steady state stress as a function of slip rate for several values of $a < b$. The steady state stress reaches a minimum at a velocity of

$$V_{\tau\text{-}min} = V_c \frac{b-a}{a}. \quad (5)$$

2.2. Strip Model Geometry

[11] At the slip speeds relevant for slow slip events, the dynamic component of the elastic stress is far smaller than the changes in stress associated with friction, and the frictional strength of the fault is equal to the static elastic stress. That stress can be written as a function of the slip in the slow slip region and its surroundings. To simplify its calculation,

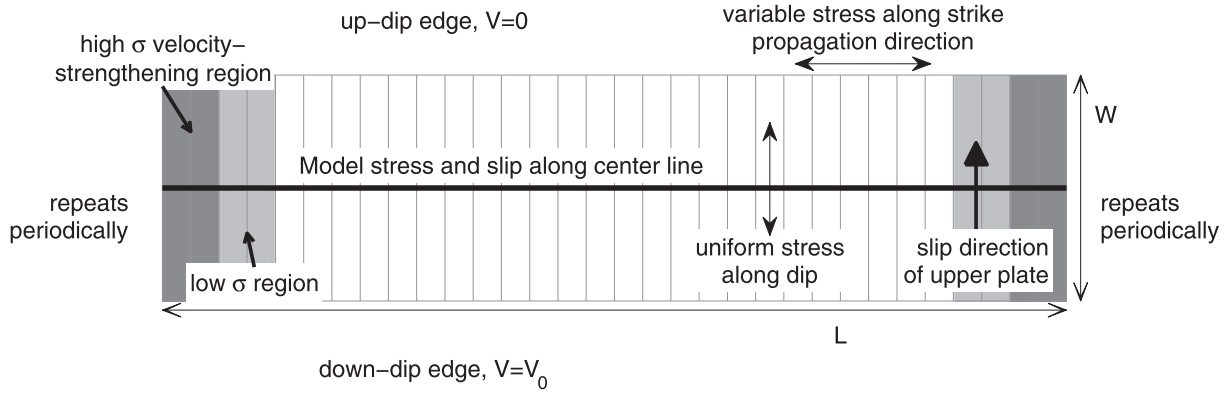

Figure 2. Strip model geometry used for elasticity calculations. We assume that stress within the slow slip region is uniform along dip and model slip along the central (horizontal) line. The fault slips at the plate rate V_0 downdip of the slow slip region and is locked updip. The model repeats periodically along strike (horizontally). See text for details.

we consider a simplified geometry in our models. The plate interface is a plane in a full space, and the slow slip region is an elongate rectangle on that plane. It has along-dip length W and along-strike length L, as illustrated in Figure 2.

[12] We are interested in the along-strike propagation of slow slip events within the specified rectangle. To investigate this propagation at a reduced computational cost, we make three more simplifying assumptions that reduce the modeled fault to a one-dimensional grid. We assume (1) that there is no slip updip of the slow slip region, (2) that the slip rate is uniform and constant downdip of the slow slip region, with value V_0, and (3) that stress is uniform along dip within the slow slip region. These assumptions determine a unique relationship between along-strike variations in stress and slip along the center line of the slow slip rectangle. This elasticity relationship is described in more detail in Appendix A1. When we couple it with the friction law, we can simulate the slip, slip rate, state, and stress along the center line indicated in Figure 2.

[13] The simulated slow slip events propagate along strike, often achieving extents much larger than the parameterized along-dip length. Slip is in the dip direction, perpendicular to the direction of propagation. For increased efficiency, the model repeats periodically in the along-strike direction. This model seems like the most reasonable one-dimensional fault geometry for investigating the along-strike propagation of slow slip events. However, it has deficiencies. For instance, the model cannot account for curvature of the rupture front, and it does not allow for along-dip variations in stress.

[14] To run the simulations, we equate the elastic stress due to slip τ_{el} (equations (A3) and (A4)) to the frictional strength from equation (1). In each time step, we use the derivative of these equations and the state evolution law (equation (2) or (3)) to update the slip rate, state, stress, and slip at each point on the fault. Updates are calculated at variable time steps using a Gear method, as implemented in ODEPACK [*Hindmarsh*, 1983].

[15] In some simulations we introduce an additional elastic stress: a small amplitude sinusoidal forcing of the form $\tau_s = A_s \sin(2\pi t/T_s)$. In those simulations we equate the total elastic stress $\tau_{el} + \tau_s$ to the frictional strength. As discussed in section 5.3, we include the sinusoidal stress because it promotes heterogeneity and facilitates more frequent nucleation of slow slip events. Its magnitude is small: 0.01 to 0.05 times the event stress drops, so it has a minor effect on other aspects of the simulation. We will not investigate this stress in the context of tidal or seasonal loading.

2.3. Parameter Distribution

[16] On most of each modeled fault, the rate and state parameters a and b are uniform with a/b between 0.6 and 0.9. However, there is a small region with width 0.25 to $0.5W$ which also obeys equation (1) but has $a > b$, as illustrated in Figure 2. b is the same in this region as on the rest of the fault, but $a - b$ here is equal to $b - a$ elsewhere. The normal stress in this $a > b$ region is a factor of 10 larger than on the bulk of the fault. These properties encourage this

Table 1. List of Notations Used

Term	Description
a	direct effect coefficient
A_s	amplitude of sinusoidal forcing
b	evolution effect coefficient
δ_c	slip-weakening displacement
D_c	length scale of slip required for state evolution
$\Delta\tau_{p\text{-}r}$	peak to residual stress drop
f^*	reference coefficient of friction
μ	shear modulus
ν	Poisson's ratio
L	along-strike length of the model domain
L_b	$D_c\mu/(b\sigma)$, a length scale for slip rate localization
R	size of the region above steady state
σ	effective normal stress
$\tau_{ss\text{-}min}$	minimum steady state stress
θ	state
θ_i	state ahead of the propagating front
$\dot{\theta}_m$	mean rate of change of state in the inter-slow slip period
T_s	period of sinusoidal forcing
V	slip rate
V_{max}	maximum slip rate in a propagation front
V_{prop}	propagation rate
V_c	cutoff velocity
$V_{\tau\text{-}min}$	minimum steady state stress velocity ($V_c(b-a)/a$)
V_0	slip rate imposed downdip of the slow slip region
V^*	reference slip rate
W	along-dip length of the fault

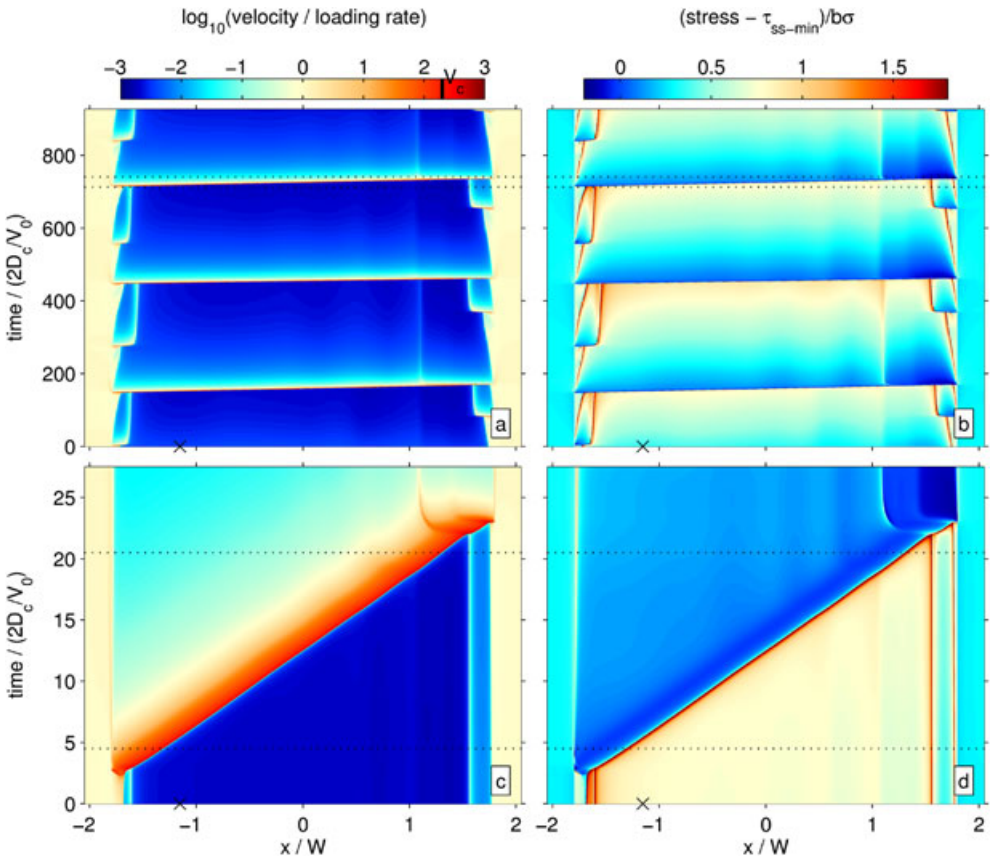

Figure 3. (a) Slip rate and (b) stress over the course of three slow slip events. The y axis is normalized time, and the x axis is distance along strike. The entire model domain is shown. The fault repeats periodically along strike, so the section with $a > b$ wraps around the edge of the plot. The beige color in that section in Figure 3a indicates steady slip at rates close to $V_0/2$. The rest of the fault slips slowly during the inter-slow slip period (blue color in Figure 3a) but quickly during slow slip events (redder colors). The x indicates the location from which we take the velocity and stress for plotting in Figures 5a–5c. (c) Slip rate and (d) stress during the time period delimited by the dotted lines in Figures 3a and 3b. The event nucleates near the velocity-strengthening section and propagates steadily "along strike" from left to right. Dotted lines in Figures 3c and 3d bound the time period for which we plot snapshots in Figure 4. This aging law simulation uses $a/b = 0.8$, $W/L_b = 500$, has a sinusoidal load with amplitude $A_s = 0.005b\sigma$ and period $T_s = 10D_c/V_0$, and has no low-normal-stress region.

part of the fault to slide at a steady rate during and between the slow slip events. The nearly steady slip during the inter-slow slip period allows for more frequent nucleation of slow slip events near the region with $a > b$. To further promote frequent nucleation, in some simulations we make the normal stress in the areas adjacent to the region with $a > b$ a factor of 3 or 10 smaller than that on the bulk of the fault. These low-normal-stress regions have size 0.125 to $0.25W$ and $a < b$. Their role in encouraging nucleation will be discussed further in sections 4.2 and 5.3.

[17] If the model equations are normalized, it can be shown that the simulation results are fully determined by the ratios a/b, W/L_b, L/W, V_0/V_c, ν, V_0T_s/D_c, and $A_s/b\sigma$, and by the properties of the velocity-strengthening and low-normal-stress regions [*Hawthorne*, 2012, section 3.10]. Here ν is Poisson's ratio and the length scale $L_b = D_c\mu/b\sigma$. A list of notations is provided in Table 1. In most of the simulations presented here, we use $V_c/V_0 = 100$, but in some simulations, V_c/V_0 is 10^3 or 10^4. In all simulations, Poisson's ratio $\nu = 0.25$ and $V_0T_s/D_c = 10$. The remaining parameters vary among the simulations. The most important parameters turn out to be W/L_b and a/b, so we will focus on their effects.

[18] In our simulations, W/L_b is between 125 and 1000. The upper bound is constrained by computational resources, while the lower bound is chosen because when W/L_b is too small, the simulation behavior enters a regime that seems inappropriate for the observed slow slip events (section 5.4). L/W is between 4 and 8, and $A_s/b\sigma$ is between 0 and 0.015.

[19] The smallest length scale that needs to be resolved in our models is L_b for the aging law and several times smaller than that for the slip law [e.g., *Ampuero and Rubin*, 2008; *Perfettini and Ampuero*, *Perfettini and Ampuero*]. In our simulations, the grid spacing in the region with $a < b$ is at least 8 points per L_b when using the aging law and 40 points per L_b when using the slip law. We do not refine the grid spacing in the region with $a > b$, even though the higher normal stress implies a smaller L_b. There are no locally high slip rates in that region that need to be resolved.

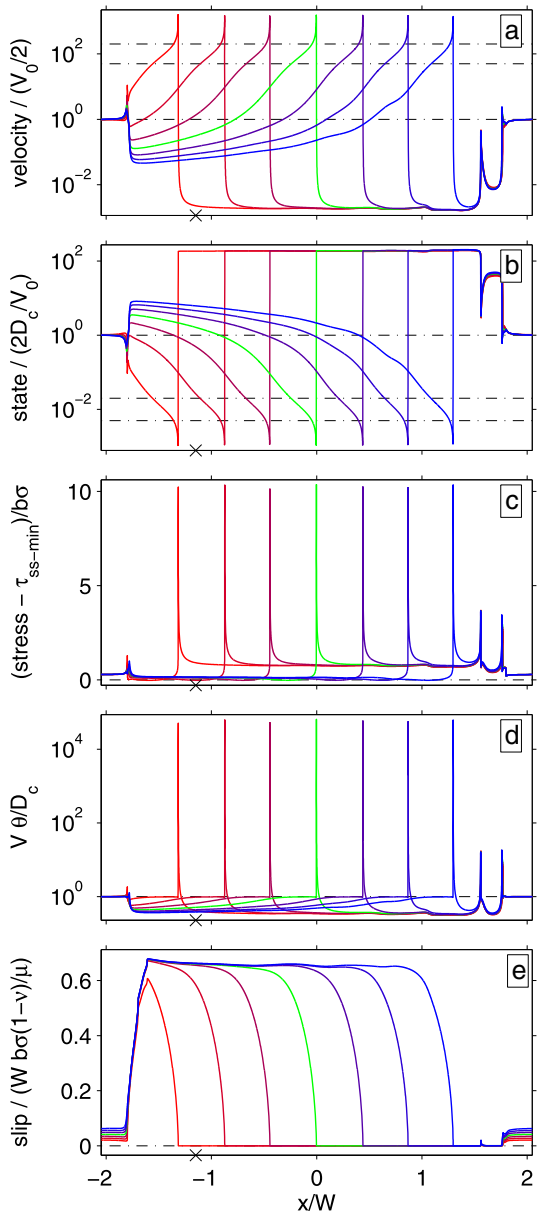

Figure 4. Snapshots of (a) velocity, (b) state, (c) stress, (d) $V\theta/D_c$, and (e) slip during part of the slow slip event shown in Figures 3c and 3d. The event propagates steadily "along strike" from left to right, with little change in the translated profiles. Snapshots are approximately equally spaced in time, which progresses from red to blue. Zero slip is defined as the slip profile that had accumulated just before this event started. The horizontal dashed-dotted line in Figure 4e marks zero slip. Dashed-dotted lines in Figure 4a indicate, from top to bottom, V_c, $V_{\tau\text{-min}}$, and $V_0/2$. Dashed-dotted lines in Figure 4b indicate, from bottom to top, D_c/V_c, $D_c/V_{\tau\text{-min}}$, and $D_c/(V_0/2)$. The x's indicate the location for which we plot stress and velocity in Figure 5. The horizontal dashed-dotted line in Figure 4c indicates the minimum steady state stress. The horizontal dashed-dotted line in Figure 4d indicates $V\theta/D_c = 1$.

3. Description of Events

[20] As has been found in previous studies [*Shibazaki and Iio*, 2003; *Shibazaki and Shimamoto*, 2007; *Shibazaki et al.*, 2010, 2012], simulations run using the model described above exhibit slow slip events. A number of them can be seen in Figures 3a and 3b, where we plot the slip rate and stress during part of one simulation. During the events, slip rates reach values slightly larger than $V_{\tau\text{-min}}$, the velocity at the transition from velocity weakening to velocity strengthening. Since $V_{\tau\text{-min}} = V_c(b - a)/a$ (equation (5)), this is equivalent to saying that the slip rates are around the cutoff velocity V_c.

3.1. Steady Propagation and Velocity Decay in the Strip Model

[21] In many simulations, such as that shown in Figure 3, large slow slip events rupture the entire fault at relatively regular intervals. These events nucleate adjacent to the section with $a > b$. They then propagate across the fault at an approximately steady rate, as seen in Figures 3c and 3d. As shown in Figure 4, the profiles of velocity, stress, state, and $V\theta/D_c$ are simply translated along the fault during this propagation.

[22] The steady propagation arises because of the strip model geometry. The parameterized updip and downdip edges constrain the local slip. This makes the stress at a given location along strike insensitive to slip in regions more than W away, and therefore insensitive to the along-strike size of the propagating event. Roughly similar steady propagation was seen in some events in the 2-D fault models of *Shibazaki and Shimamoto* [2007] and *Shibazaki et al.* [2010] when the slow slip region was strip-like, and in the models of *Bar Sinai et al.* [2012], who imposed an elasticity length scale perpendicular to the fault plane.

[23] In the strip model geometry, if the stress drop in an event is roughly uniform along strike, the slip in that event is also uniform. As such an event propagates, slip accumulates quickly near the front but tends to a constant well behind it, as seen in Figure 4e. The slip rate is thus large near the propagating front but decays behind it. It decreases by several orders of magnitude over a distance shorter than W, as seen in Figure 4a.

[24] In a propagating uniform stress drop event, the length scale for the decay of slip rate is W. However, the stress drop is not quite uniform with the chosen friction law. As a result, the length scale for the decay of slip rate varies by about a factor of 2 among the events in our simulations. It is larger when the ratio of the maximum velocity to the minimum steady state stress velocity $V_{\tau\text{-min}}$ is larger.

3.2. Evolution of Slip Behavior Behind the Rupture Front

[25] In order to better understand the properties of the propagating slow slip event, we consider the evolution of stress, slip rate, and state at a single location as the slow slip event approaches that point and ruptures through it. Figure 5a shows the stress and velocity at the location indicated by an x in Figures 3 and 4 over the course of three slow slip events. Figure 5d shows one snapshot of stress as a function of distance along strike. One can imagine that as the front in Figure 5d propagates to the right, the point

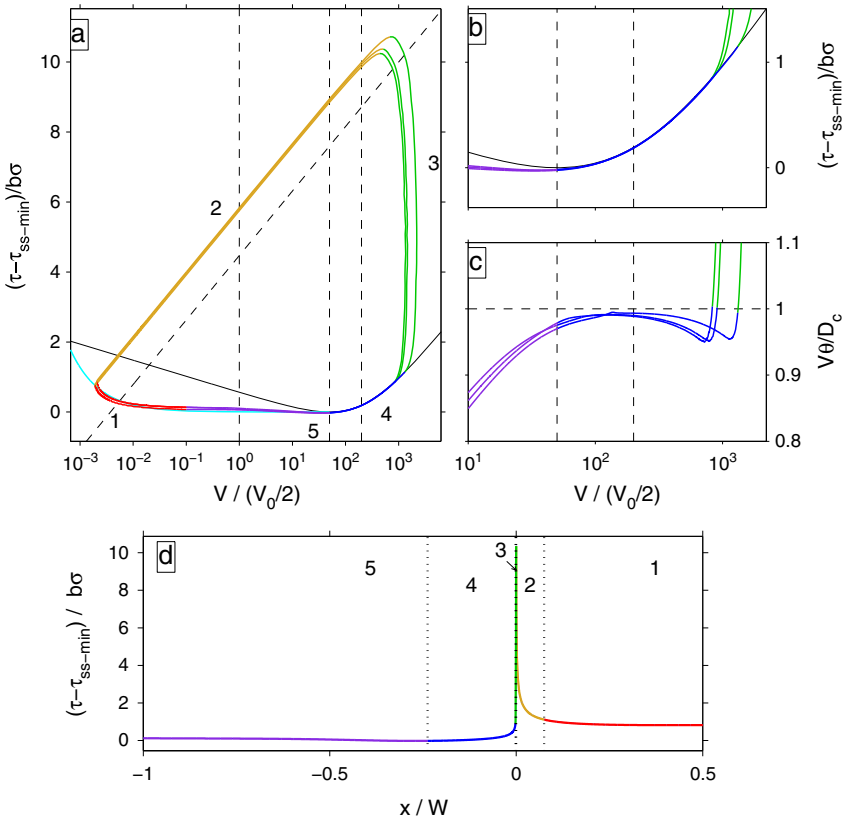

Figure 5. (a) Multicolored curve: stress versus slip rate at the location indicated by the x in Figures 3 and 4 during three slow slip events. Time progresses clockwise around the stress-velocity loop. The numbers and colors indicate portions of the slow slip cycle referred to in the text, though the boundary between segment 5 (in purple) and segment 1 (in red) is arbitrary. The solid black curve illustrates the steady state stress. The cyan curve shows the predicted evolution of stress and slip rate during the inter-slow slip period, assuming a constant loading rate and $\dot{\theta} = 0.3$. Vertical dashed lines indicate, from left to right, $V_0/2$, $V_{\tau\text{-min}}$, and V_c. The diagonal dashed line has constant state. (b) Expansion of the part of the stress-velocity curve when this location is near steady state. (c) $V\theta/D_c$ in that part of the cycle. The fault is close to but slightly below steady state in this period. Time progresses from top right to bottom left in Figures 5b and 5c. Vertical dashed lines in Figures 5b and 5c indicate, from left to right, $V_{\tau\text{-min}}$ and V_c. (d) One snapshot of stress as a function of distance along strike, as in Figure 4c. The x axis is shifted so that zero is the location of maximum stress. The colors and numbers indicate which portion of the stress-velocity curve each region is currently in. The vertical dashed lines divide those segments.

depicted in Figure 5a moves from right to left through the representative stress profile.

[26] Before the event begins, most of the fault is below steady state ($V\theta/D_c < 1$) and is slipping slowly. The stress and velocity at the point of interest plot in the lower left corner of Figure 5a, along the segment labeled with a number 1 and colored red. This location is near the center of the fault, and the stress and velocity are largely unperturbed by the nucleation of the slow slip event near the section with $a > b$. It slips at rates well below V_0 until the front arrives.

3.2.1. Near-Tip Region

[27] When the slow slip front does arrive at the location of interest, the stress there increases quickly. There is minimal state evolution during this rapid increase, so the increase in frictional strength is taken up by an increase in slip rate (segment 2 in Figures 5a and 5d, in yellow). This part of the fault is pushed far above steady state, resulting in the peaks in $V\theta/D_c$ visible in Figure 4d.

[28] By the time this location reaches its maximum stress, the velocity is high, and state evolves quickly toward steady state (segment 3 in Figure 5, in green). In later sections, it will be useful to know the stress drop that occurs during this state evolution: the peak to residual stress drop $\Delta\tau_{\text{p-r}}$. In Appendix B1 we estimate both the maximum stress and the stress when the fault reaches steady state, as a function of the maximum velocity $V_{\max}$ and the state ahead of the front θ_i. Their difference, $\Delta\tau_{\text{p-r}}$, is within about 5% of (equation (B3))

$$\Delta\tau_{\text{p-r}} \approx b\sigma\left[\log\left(\frac{V_c\theta_i}{2D_c}+1\right)-\log\left(\frac{2V_c}{V_{\max}}+1\right)\right]. \quad (6)$$

[29] Because state evolves more quickly than velocity in the near-tip region, it is possible to obtain analytical approximations for the evolution of stress with displacement. This is done in Appendix B1 (equations (B1) and (B2)). These expressions determine the slip-weakening distance δ_c: the amount of slip accumulated during the rapid state evolution.

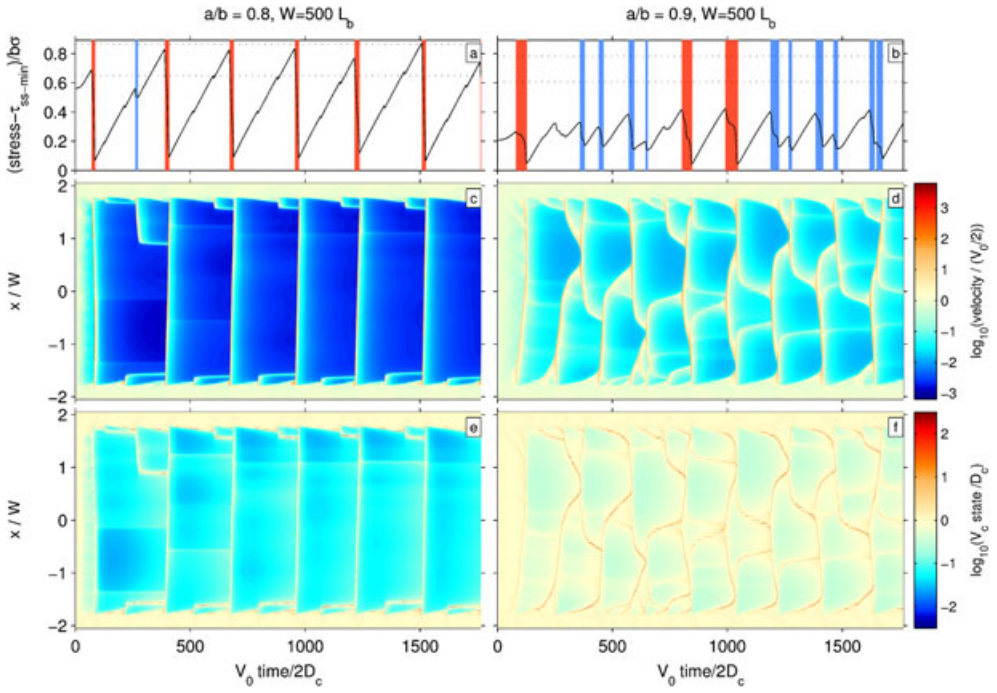

Figure 6. (left column) Illustration of a simple periodic aging law simulation with a/b = 0.8, W/L_b = 500, no low-normal-stress region, and no sinusoidal forcing. (a) Mean stress in the velocity-weakening region as a function of time. (c) Slip rate and (e) $V\theta/D_c$ as a function of time (x axis) and distance along strike (y axis). In this simulation, a number of events nucleate near the section with $a > b$, and large events periodically rupture the entire fault. (b,d, and f) The same as Figures 6a, 6c, and 6e, respectively, but for a simulation with more complicated behavior. For this simulation, a/b = 0.9 but all other parameters are identical to the simulation in the left column. Events nucleate at many locations, and large events do not show a consistent periodicity. Horizontal lines in panels Figures 6a and 6b indicate the stress drops predicted by the K = 0 approach (section 5.2), assuming maximum velocities of $10V_{\tau\text{-min}}$ and $30V_{\tau\text{-min}}$ for the lower and upper lines, respectively

As for standard rate and state friction [e.g., *Ampuero and Rubin*, 2008], $\delta_c \approx D_c\Delta\tau_{\text{p-r}}/b\sigma$ for the aging law and $\delta_c \approx D_c$ for the slip law.

[30] Elasticity requires that the slip-weakening distance δ_c scale with $(\Delta\tau_{\text{p-r}}/\mu)R$, where R is the size of the near-tip region [e.g., *Rice*, 1980]. In rate and state simulations, it is common for R to scale roughly with $L_b = D_c\mu/b\sigma$, as defined in section 2.3 [e.g., *Rubin and Ampuero*, 2005; *Ampuero and Rubin*, 2008]. Indeed, we find that the size of the region between the maximum stress and the first point to reach steady state is 0.9 to 1.1 L_b in aging law simulations and 3 to 4.5 $L_b b\sigma/\Delta\tau_{\text{p-r}}$ in slip law simulations. 90% of the peak to residual stress drop occurs in a region with size 0.6 to 0.7 L_b in aging law simulations and 1.3 to 1.6 $L_b b\sigma/\Delta\tau_{\text{p-r}}$ in slip law simulations. These sizes and their scalings are similar to those found for standard velocity-weakening rate and state friction [e.g., *Ampuero and Rubin*, 2008].

[31] The size of the near-tip region R can also be written as $V_{\text{prop}}\Delta t$, where V_{prop} is the propagation rate and Δt is the time that any point spends in the near-tip region. With this definition of Δt, the slip-weakening distance δ_c scales as $V_{\text{max}}\Delta t$. The relation $\delta_c \sim (\Delta\tau_{\text{p-r}}/\mu)R$ then implies that

$$V_{\text{prop}} = \alpha V_{\text{max}} \frac{\mu}{\Delta\tau_{\text{p-r}}} \tag{7}$$

[*Ida*, 1973; *Shibazaki and Shimamoto*, 2007; *Ampuero and Rubin*, 2008]. Here α is a constant accounting for the shape of the local slip profile. This relation holds in our simulations, where $\alpha \approx 0.50 - 0.55$ for the aging law and $\alpha \approx 0.57 - 0.65$ for the slip law.

[32] Note that the size of the near-tip region R is less than $0.01W$ in our simulations. Elasticity in this region is then well approximated by an antiplane strain model that is independent of W, so long as the propagating front is straight on length scales much longer than R. Because of this, the properties of the near-tip region would remain unchanged if the strip model geometry were modified.

3.2.2. Region Near Steady State

[33] Just outside the region above steady state, the velocity is about $V_{\text{max}}/2$ and decreasing. $V\theta/D_c$ also continues to decrease slightly. However, it levels off to a value between 0.9 and 0.999 within a few L_b behind the front. Here begins a relatively large region where the fault is close to but slightly below steady state (the blue portion of Figure 5d). In this region the slip rate and stress gradually decrease with distance from the front. They closely follow the velocity-strengthening section of the steady state curve, as seen in segment 4 in Figure 5a and in Figures 5b and 5c.

[34] The fault remains near steady state until the slip rate falls below $V_{\tau\text{-min}}$. In cycle simulations, this occurs between

$0.1W$ and $0.5W$ behind the front. The edge is closer to the front when the maximum velocity is smaller, since in that case a small decrease in slip rate brings the fault to its minimum steady state stress velocity ($V_{\tau\text{-min}}$).

[35] It is difficult to obtain analytical expressions for the gradual decay of stress and velocity behind the front. However, in Appendix C, we obtain simple numerical approximations that are reasonably accurate within about $0.1W$ of the front. These approximations depend only on the model parameters, the maximum velocity, and the initial state. They will be useful in section 5.2.

3.2.3. Region Below Steady State

[36] Farther behind the front, the slip rate falls below $V_{\tau\text{-min}}$, and the fault falls below steady state (segment 5 in Figure 5, in purple). State continues to increase, and the stress either remains the same or increases by a few to 30% of the initial stress drop. The stress recovery is interesting, because regions with recovered stress can slip again if they are perturbed. The parameters controlling its magnitude are considered by *Hawthorne* [2012].

4. Inter-Slow Slip Behavior and Nucleation

4.1. Inter-Slow Slip Loading and Evolution

[37] By the end of a major slow slip event, the stress throughout the velocity-weakening region has fallen to a value near the minimum steady state stress $\tau_{\text{ss-min}}$. The slip rates have fallen to values well below the loading rate V_0. Since the downdip slip rate is assumed to be V_0 and uniform along strike (see section 2.2), the slow slip region is loaded at a steady rate during the inter-slow slip period. Stress increases at an approximately uniform and constant rate of $\mu(1-\nu)^{-1}V_0/2W$.

[38] State also increases in the inter-slow slip period, as $V\theta/D_c$ is between 0.2 and 0.8 on most of the fault during that time. We find that except for a short interval after an event, $\dot{\theta}$ changes by less than a factor of 2 during the inter-slow slip period. The evolution of θ can be reasonably approximated by assuming that $\dot{\theta}$ is equal to a constant, which we call $\dot{\theta}_m$.

[39] Since we wish to know the value of state in the inter-slow slip period, not just its rate of change, we assume that at the end of the last slow slip event, state was equal to $D_c/V_{\tau\text{-min}}$. The state at every location on the fault approaches that value at some point during each slow slip event. The change in state associated with the nearly linear increase quickly becomes greater than $D_c/V_{\tau\text{-min}}$, however, so the initial value has only a minor influence on our estimate of state late in the inter-slow slip period.

[40] To demonstrate the accuracy of at least one set of stress and state predictions, we plot the predicted evolution of stress and velocity along with the simulated values in Figure 5a (cyan curve). Here we have chosen $\dot{\theta}_m = 0.3$. In this case and in most other simulations checked, the predictions reasonably match the simulated stress and velocity. However, the chosen value of $\dot{\theta}_m$ does influence the quality of the fit. $\dot{\theta}_m$ varies from 0.2 to 0.8 among the simulations considered. It is smaller for larger a/b and smaller W/L_b, but we do not have a simple quantitative understanding of those changes.

4.2. Nucleation Near the Velocity-Strengthening Section

[41] The approximations given above break down on one part of the fault: near the section with $a > b$. That section slips at rates near the loading rate ($V_0/2$) throughout the inter-slow slip period (see Figure 3a). This steady slip provides an additional load on its immediate surroundings. As a result, the velocity-weakening ($a < b$) regions that are adjacent to the section with $a > b$ reach a steady state stress before the rest of the fault, and slow slip events nucleate there. As seen in Figure 3, some of the nucleated events rupture the entire fault, but many fail after propagating only a short distance.

[42] If this localized nucleation occurs very infrequently in a given simulation, all of the events rupture the entire fault. Those events can have much larger stress drops and slip rates than those in the simulations shown here. Further, after these events rupture the entire along-strike region, the whole area continues to slip at rates well above V_0 for some time [*Hawthorne*, 2012]. This seems to contrast with observed events. Geodetic and tremor observations suggest that the slip rate decays to small values over length scales shorter than the along-dip length [e.g., *Wech et al.*, 2009; *Bartlow et al.*, 2011; *Dragert and Wang*, 2011].

[43] As noted in sections 2.2 and 2.3, we introduce two features to ensure that slow slip events nucleate frequently in the simulations presented in this paper. First, in some simulations, we reduce the normal stress in the velocity-weakening regions surrounding the velocity-strengthening section. The reduced normal stress allows loading from slip in the velocity-strengthening ($a > b$) section to bring this part of the fault to steady state more quickly. Second, we apply a small sinusoidal variation in shear stress in addition to the elastic stress due to slip. While this stress is never more than a few percent of the stress drops in large events, it increases the temporal and spatial heterogeneity in the slip rate.

5. Stress Drop Estimates

[44] Many simulations, including the one shown in Figure 3, exhibit large events that rupture the entire fault at fairly regular intervals. A second such simulation is shown in the first column of Figure 6. On the other hand, some simulations exhibit a more complicated series of events, often with no obvious periodicity. The second column of Figure 6 shows one of these simulations. We will discuss the behavior of the complicated simulations in section 5.4. In sections 5.1 and 5.2, we investigate the recurrence interval of large events in the periodic simulations, so that we may compare with the recurring slow slip events in Cascadia [e.g., *Dragert et al.*, 2001; *Szeliga et al.*, 2008] and parts of Japan [e.g., *Obara et al.*, 2004; *Hirose and Obara*, 2010].

5.1. Stress Drops From the Simulations

[45] To analyze our simulation results, we use the automated event detection algorithm described by *Hawthorne* [2012]. We define a "major" event as one in which there is a stress drop of at least $0.02b\sigma$ on at least 80% of the region with $a < b$. In Figures 6a and 6b major events are marked with red bars while smaller events are marked with blue bars. As an estimate of the event stress drop, we take the average

of the stress drop in regions where stress has decreased, plus a small adjustment: $\mu(1-\nu)^{-1}V_0\delta t/2W$, where δt is the duration of each event. This final addition accounts for the load from continued downdip slip during the event. We include it here because it would be included in geodetic estimates of the accumulated moment. It changes the results by 15% or less.

[46] Figure 7 shows the mean stress drops in major events for simulations with a range of W/L_b and a/b. Several trends are visible. First, events simulated with the slip law (Figure 7b) tend to have much smaller stress drops than those simulated with the aging law (Figure 7a). Second, the stress drops decrease with increasing along-dip length W (plotted on the x axis).

[47] The stress drop is insensitive to some model parameters. The crosses and pluses indicate simulations with V_c/V_0 of 10^3 and 10^4, respectively. Except for a few outliers with a/b of 0.6, the stress drops in those simulations are the same as those in simulations with $V_c/V_0 = 10^2$. Also, except for one obvious outlier in Figure 7b, the value of the normal stress in the low-normal-stress region (symbol type) and the presence or lack of sinusoidal forcing (open versus filled) have little effect on the stress drop. We have not indicated the values of the along-strike length L or the size of the velocity-strengthening section in Figure 7. These parameters also do not systematically affect the stress drop.

[48] When plotting our results, we have chosen to normalize the along-dip length by L_b and the stress drop by $b\sigma$, because this normalization does the best job of collapsing the results for simulations with a range of a/b and W. Simulations with a/b of 0.9, and to a lesser extent, with a/b of 0.8, do appear to have slightly but systematically lower stress drops relative to $b\sigma$. We will discuss the reasons for the these smaller stress drops at the end of section 5.4. In that section we will also investigate the behavior of simulations with a/b of 0.9 and W/L_b of 125 and 250. No stress drops are plotted for the simulations run with those parameter sets because they do not exhibit periodic large events.

5.2. Understanding the Stress Drops

[49] In order to quantitatively understand the stress drops in large events, we note that many events nucleate near the velocity-strengthening section, but only a fraction of them propagate across the entire fault. This suggests that we need to identify why some events can propagate and others cannot. We consider a requirement for propagation that is based on properties of the near-tip stress field. This requirement closely parallels an energy balance argument. During propagation of a slow slip event, the strain energy released by slip must equal the fracture energy. The strain energy release can be thought of as a function of the stress drop and along-dip extent of the event. The fracture energy, which is dissipated largely in the near-tip region, is essentially the work done during the transition from "static" to "kinetic" friction.

[50] *Hawthorne* [2012] used the energy balance requirement to predict the stress drop $\Delta\tau$ for our model. That estimate is indicated by the black dashed curves in Figure 7, and it does a relatively good job of reproducing the trends in the stress drops taken from the simulations, as will be discussed in section 5.2.3. However, it involves a free parameter that must be empirically tuned to match the stress drops from the simulations. Here we wish to avoid the need

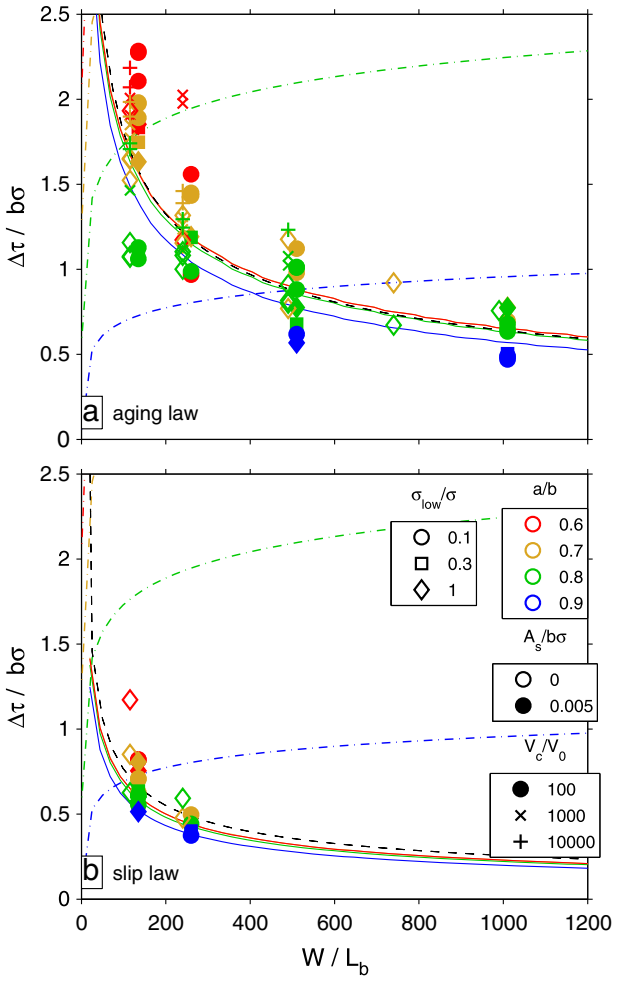

Figure 7. Mean stress drops in major events as a function of the along-dip length W in simulations using (a) the aging law and (b) the slip law. For all colored symbols and curves, color corresponds to a/b. The crosses and pluses are for simulations with V_c/V_0 of 10^3 or 10^4, a normal stress in the low-normal-stress region that is 0.1 times that on the bulk of the fault, and no sinusoidal forcing. The remaining points are for simulations with V_c/V_0 of 100. Among those results, symbol type indicates the normal stress in the low-normal-stress region. Filled symbols have sinusoidal forcing with half-amplitude $0.005b\sigma$. Open and filled symbols are offset for visibility but were run with the same values of W/L_b. The colored solid curves indicate the predicted stress drops using the stress intensity factor approach. The black dashed curves indicate the predicted stress drops using an energy balance approach (equation (13), as estimated by *Hawthorne* [2012]). The colored dashed-dotted curves indicate $\Delta\tau_{ss}$, the predicted stress increase since the last event required for the fault to reach steady state (section 5.4). The $\Delta\tau_{ss}$ for $a/b \leq 0.7$ are mostly too large to fit on the plot.

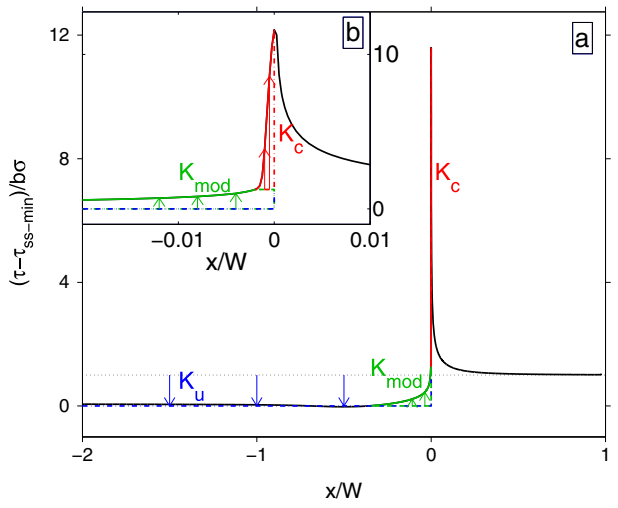

Figure 8. (a) Illustration of stress profiles associated with each of the defined contributions to K. The combined solid curve is the stress in the propagating event. The colored sections indicate $\Delta\tau_c$, $\Delta\tau_{\mathrm{mod}}$, and $\Delta\tau_u$: the stress profiles contributing to K_c, K_{mod}, and K_u, respectively. The stress changes for each component are relative to the beginning of the colored arrows. The component profiles sum to the stress change in the propagating event, $\tau(x)-\tau_{\mathrm{init}}$, as required in equation (8). This profile was extracted from a steadily propagating simulation (described in Appendix E1) with $a/b = 0.8$, $W/L_b = 500$, stress drop $b\sigma$, and state ahead of the front $\theta_i = 10^5 D_c/V_c$. (b) Expansion of the near-tip region, illustrating the stress profile associated with K_c.

for that empirical fit. Therefore, we consider a slightly different requirement for the propagation of an event: that stress remain finite at the tip of the propagating rupture. Instead of balancing the strain and fracture energies, we balance the positive and negative contributions to a potential stress singularity at the rupture tip.

5.2.1. Stress Intensity Factor Approach

[51] The stress intensity factor K is a measure of the singularity in stress at the tip of a propagating rupture. When $K \neq 0$, the stress at the tip is infinite. Infinite stresses are not permitted by the friction law, so K must equal zero. The positive contributions to the stress singularity associated with the stress drop are canceled by the negative contributions associated with the large near-tip stresses [e.g., *Barenblatt*, 1962]. To understand more explicitly how $K = 0$ constrains the stress profiles $\tau(x)$ in the propagating events, note that K can be written as a function of the stress change behind the front:

$$K = -\int_0^{L_s} c_k(x)(\tau(x) - \tau_{\mathrm{init}})\mathrm{d}x. \tag{8}$$

Here τ_{init} is the stress in the region of interest before the slow slip event arrives. We use only a single value for τ_{init} since this initial stress is roughly uniform. L_s is the along-strike extent of the region with nonzero slip, and x is distance behind the tip. Here the "tip" is a location ahead of which there is zero slip. As discussed in Appendix B, it is close to the location of the maximum stress. The $c_k(x)$ in equation (8) are coefficients that depend on the strip model geometry and on L_s. We determine the values of $c_k(x)$ for the chosen strip model geometry numerically, as described in Appendix A2.

[52] In most of the region behind the front, stress has decreased from its initial value, and $\tau(x) - \tau_{\mathrm{init}} < 0$. This results in a positive contribution to K that plays a role analogous to the strain energy release. On the other hand, the stress $\tau(x)$ is larger than τ_{init} in the near-tip region, where state is still decreasing from the large values of the inter-slow slip period. This results in a negative contribution to K that plays a role analogous to the fracture energy.

[53] An event can rupture the entire fault when it is possible to have $K = 0$: when the positive and negative contributions to the near-tip stress field have equal magnitudes. The positive contribution to K scales with the available stress drop. This is near zero just after a slow slip event and then increases roughly linearly with time during the inter-slow slip period, as stress accumulates from the steady slip downdip of the slow slip region. The negative contribution to K depends on the value of state: on how much the fault has healed since the last event. The fault heals most quickly just after a slow slip event. As a result, the potential negative contribution to K is larger than the potential positive contribution not long after a slow slip event. Later in the inter-slow slip period, however, the positive contribution increases more rapidly than the negative contribution and events can rupture the entire fault.

[54] In the next few sections, we estimate the positive and negative contributions to K for an event that attempts to rupture the fault at time t after the previous event. If small events nucleate and attempt to propagate frequently enough, the first time when the predicted contributions sum to zero will be the estimated recurrence interval Δt. Since stress accumulates at a roughly constant rate during the inter-slow slip period, the stress drop in recurring events is the stress that accumulates in that interval: $\mu(1-\nu)^{-1}V_0\Delta t/2W$.

[55] We should note that when we assess whether an event can propagate across the entire fault, we will assume that it has already achieved an along-strike extent comparable to W. The strip model geometry does not provide a good framework for examining the properties of events when they are smaller. The assumption here is that events repeatedly nucleate and grow adjacent to the steadily sliding region with $a > b$, as described in section 4.2. We determine whether those events can continue to grow to sizes much larger than W.

5.2.2. Contributions to K

[56] In the last section, we described K as the sum of one negative and one positive contribution. We actually divide K into three contributions: K_c, K_u, and K_{mod}. K_c is a negative contribution from the high stresses in the near-tip region, and K_u is a positive contribution from a uniform stress drop behind the propagating front. K_{mod} is a negative contribution. It can be thought of as modifying the positive contribution associated with the stress drop, as it accounts for the gradual decay of stress behind the front, in the region near steady state.

[57] To define these contributions precisely, we note that K is a linear function of the stress change behind the front (equation 8). We can then write K as the sum of contributions from three stress change profiles, so long as those profiles sum to $\tau_{\mathrm{init}} - \tau(x)$. We refer to the three stress change

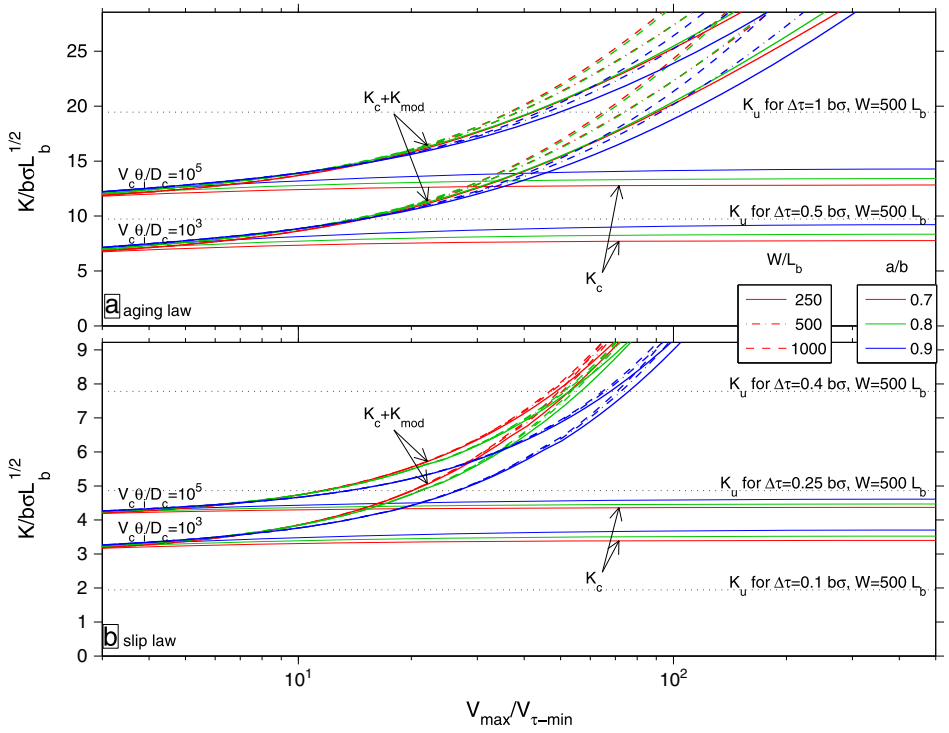

Figure 9. Predicted value of the negative contributions to K as a function of maximum slip rate V_{max} for the (a) aging law and (b) slip law. The four sets of curves labeled K_c indicate $|K_c|$. The remaining sets of curves indicate $|K_c + K_{mod}|$. $|K_c|$ increases weakly with slip rate at low velocities and tends to a constant at higher velocities, while $|K_c + K_{mod}|$ depends strongly on slip rate at higher velocities. The lower sets of curves are for a smaller initial state θ_i, with $V_c\theta_i/D_c = 10^3$, while the upper sets of curves are for $V_c\theta_i/D_c = 10^5$. The along-dip length W and a/b are indicated in the legend. The horizontal dashed lines labeled K_u are the predicted (positive) contributions to K from a uniform stress drop for the parameters indicated. The maximum velocities in events with those parameters can be obtained from the intersection of the dotted lines with the $|K_c + K_{mod}|$ curves.

profiles as $\Delta\tau_c(x)$, $\Delta\tau_u$, and $\Delta\tau_{mod}(x)$, respectively. Their contributions to K can be calculated from

$$K_i = -\int_0^{L_s} c_k(x)\Delta\tau_i(x)\mathrm{d}x, \tag{9}$$

where i is c, u, or "mod". The stress change profiles we consider are illustrated in Figure 8, where the solid lines depict a stress profile taken from a simulation.

[58] We begin by investigating the contribution K_c, associated with the stress change profile $\Delta\tau_c$. K_c comes from the large stresses near the tip associated with overcoming near-static friction. We define $\Delta\tau_c$ as the difference between the stress in the region where the fault is above steady state and the steady state stress reached at its edge (red curve and arrows in Figure 8). $\Delta\tau_c$ is zero outside of that region. Since the fault is well above steady state in most of the region that contributes to K_c, and since the slip rate changes slowly relative to state, we can use the friction law to obtain analytical approximations for $\Delta\tau_c$ and therefore for K_c. In Appendix B2, we estimate that (equation (B8))

$$K_c = -\beta b\sigma\sqrt{L_b}\left[\log\left(\frac{V_c\theta_i}{2D_c}+1\right) - \log\left(\frac{2V_c}{V_{max}}+1\right)\right]^{(n-1)/2}, \tag{10}$$

where $\beta \approx 1.1$ for the aging law and $\beta \approx 1.3$ for the slip law, and $n = 2$ for the aging law and $n = 1$ for the slip law. This estimate matches the values observed in simulations to within a few percent for the aging law and to within 10% for the slip law.

[59] The value in brackets in equation (10) is equal to $\Delta\tau_{p\text{-}r}/b\sigma$, which is of the order 10 in our simulations. Because of that factor, K_c is larger for the aging law ($n = 2$) than for the slip law ($n = 1$). As seen in Appendix B2, this difference arises because the slip-weakening displacement $\delta_c \approx D_c\Delta\tau_{p\text{-}r}/b\sigma$ for the aging law but $\delta_c \approx D_c$ for the slip law (section 3.2.1 and *Ampuero and Rubin* [2008]). Rock friction experiments indicate that the slip-weakening displacement δ_c is independent of $\Delta\tau_{p\text{-}r}$ [*Ruina*, 1980; *Bayart et al.*, 2006]. To the extent that existing laboratory experiments are an adequate guide to the slow slip source region, this implies that it is more appropriate to use the slip law when calculating K_c.

[60] For both evolution laws, the peak to residual stress drop and therefore K_c depend on the value of state in the region the event is propagating into (θ_i) and on the maximum velocity (V_{max}). We illustrate the dependence of K_c on V_{max} in Figure 9. For V_{max} not too far above the minimum steady state stress velocity $V_{\tau\text{-}min}$, K_c increases as $\log(V_{max})^{n/2}$. This scaling is the same as that for standard velocity-weakening friction, as implied by the fracture energy estimates of *Rubin and Ampuero* [2005] and *Ampuero and Rubin* [2008]. At large maximum velocities, K_c tends to a value that is

independent of slip rate, essentially because $\Delta\tau_{p\text{-}r}$, depicted in the green portion of Figure 5a, tends to a constant at high slip rates.

[61] The second contribution to K that we consider is K_u. It is a positive contribution that counters the negative K_c, and it is associated with the roughly uniform stress drop in the propagating event. The corresponding stress change profile $\Delta\tau_u(x)$ is uniform in space and equal to $\tau_{ss\text{-}min} - \tau_{init}$ (blue curves and arrows in Figure 8). Here $\tau_{init} - \tau_{ss\text{-}min}$ is approximately equal to the average stress drop in the event, $\Delta\tau$. If we insert this uniform stress in equation (9) and integrate, we can note that the coefficients $c_k(x)$ decay toward zero as x gets larger than W. This implies that the contribution K_u tends toward a constant as the event grows to an along-strike extent larger than W. It approaches a value of

$$K_u \approx \psi \Delta\tau \sqrt{W}. \tag{11}$$

Here ψ is a factor that accounts for the parameterized 2-D geometry of the slow slip event [e.g., *Lawn*, 1993]. For the chosen strip model geometry and a Poisson's ratio of 0.25, ψ is 0.87 to within a few percent (see Appendix A2).

[62] The contributions K_u and K_c ignore variations in stress in the part of the slipping region near steady state. We account for this gradual decay of stress with the final contribution to K, K_{mod}. The stress change profile $\Delta\tau_{mod}(x)$ is defined as the difference between the decaying stress seen in the simulations and the final stress $\tau_{ss\text{-}min}$ assumed when computing K_u (green curves in Figure 8). As discussed in section 3.2.2, this gradual decay of stress occurs along the steady state stress-velocity curve. In Appendix C, we come up with approximations for this gradual decay that are reasonably accurate within $0.1W$ of the front. In Appendix D, we use those approximations to estimate K_{mod} as a function of the maximum velocity V_{max}, a/b, and W.

[63] The dependence of K_{mod} on these parameters is illustrated in Figure 9, where the concave up curves indicate $|K_c + K_{mod}|$. Like K_c, K_{mod} scales with $b\sigma\sqrt{L_b}$. It varies by only a small amount with a/b and W. Unlike K_c, K_{mod} depends only weakly on the maximum velocity V_{max} when V_{max} is not much larger than $V_{\tau\text{-}min}$. But when V_{max} is larger than $10V_{\tau\text{-}min}$, K_{mod} depends strongly on V_{max}.

[64] The total negative contribution $|K_c + K_{mod}|$ thus increases as $\log(V_{max})^{n/2}$ at low slip rates, as does the K_c for standard velocity-weakening friction [e.g., *Rubin and Ampuero*, 2005; *Ampuero and Rubin*, 2008]. But at high slip rates, $|K_c + K_{mod}|$ increases much faster than logarithmically. We will see in sections 5.3 and 6 that it is this strong dependence of $|K_c + K_{mod}|$ on V_{max} that causes the maximum slip rate to vary relatively little during and among the simulated events.

5.2.3. Stress Drop Predictions

[65] Using the division of K described above, the requirement that $K = 0$ during propagation can be written as

$$K_u(\Delta\tau, W) + K_{mod}(V_{max}, a/b, W, \theta_i) = -K_c(V_{max}, \theta_i), \tag{12}$$

where the parameters in parentheses are the important factors controlling the value of each contribution. Of these factors, W and a/b are constants. $\Delta\tau$ and θ_i are determined by the conditions on the fault prior to the slow slip event. We estimated them as a function of time in the inter-slow slip period in section 4.1. The only remaining unknown is V_{max}.

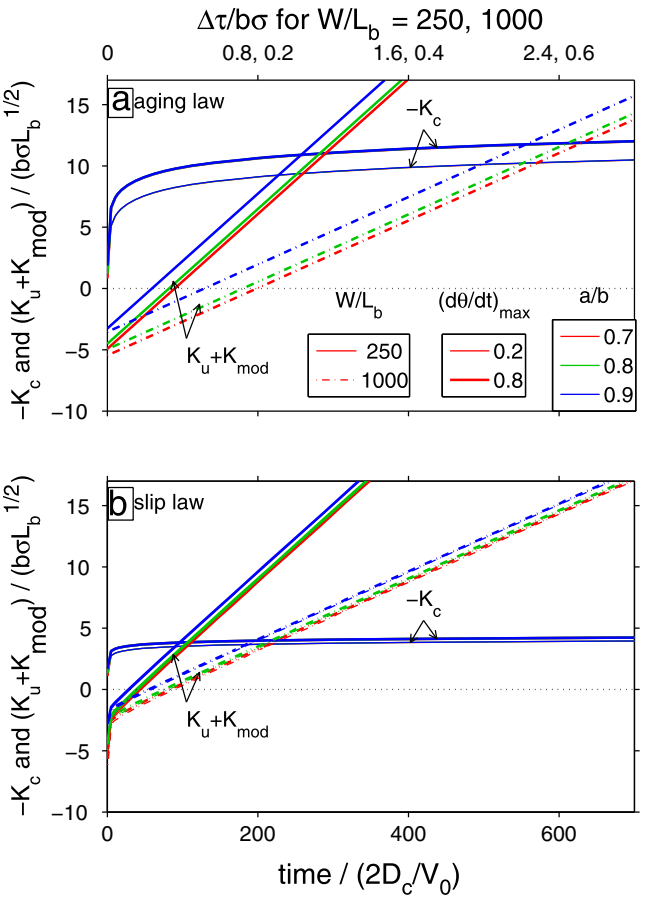

Figure 10. Predicted $-K_c$ (concave down curves) and $K_u + K_{mod}$ (approximately straight lines) for a given event as a function of the time at which it nucleates. The next event to rupture the entire fault is expected to occur when $-K_c = K_u + K_{mod}$: where these curves intersect. The stress drop in that event for a chosen W/L_b can be read off the upper axis. The calculations use either (a) the aging law or (b) the slip law.

[66] One way to think about V_{max} is as a function of the initial conditions. Indeed, if $\Delta\tau$, θ_i, and the model parameters were fixed, we could solve equation (12) for V_{max}. With this approach, V_{max} should be larger when $\Delta\tau$ is larger, at longer times after the last event. It should be smaller when the available $\Delta\tau$ is smaller. However, as discussed in section E3, events cannot propagate if V_{max} is too small. A steadily propagating event is possible only if V_{max} is larger than some minimum. To predict the recurrence intervals of our events, we assume that an event will rupture the entire fault when the initial conditions imply a maximum velocity larger than that minimum. Specifically, we will assume that $V_{max} = 30V_{\tau\text{-}min}$, as V_{max} is between 10 and $40V_{\tau\text{-}min}$ in large cycle simulation events.

[67] Figure 10 shows the values of the predicted $-K_c$ and $K_u + K_{mod}$ as a function of nondimensionalized time since the last event. Here we have used the approximations from section 4 to estimate the available stress drop and the initial state. We take the average rate of change of state $\dot{\theta}_m$ to be 0.2 or 0.8. These two values approximately span the range seen in simulations. Since $|K_c|$ increases roughly as

$(\log(V_{\max}\dot{\theta}_m t/D_c))^{n/2}$, this choice makes only a minor difference in the estimated values. As before, t is the time since the last event.

[68] The ratio of the cutoff velocity V_c to the loading rate V_0 also makes only a minor difference in the estimated values. To understand this, note that in Figure 9 K_c and K_{mod} are best written as functions of $V_{\max}/V_{\tau\text{-min}}$ and $V_{\max}\theta_i/D_c$. The ratio $V_{\max}/V_{\tau\text{-min}}$ is 10 to 40 regardless of V_c/V_0, so V_c enters $K_c + K_{\mathrm{mod}}$ only through the term $V_{\max}\theta_i/D_c \approx$ 10 to 40 $V_{\tau\text{-min}}\dot{\theta}_m t/D_c$. $|K_c|$ increases only as $(\log(V_{\max}\dot{\theta}_m t/D_c))^{n/2}$, so the dependence of $K_c + K_{\mathrm{mod}}$ on V_c/V_0 is quite weak.

[69] The next large event is expected when $-K_c = K_u + K_{\mathrm{mod}}$, at the intersection of the appropriate curves in Figure 10. For ease in reading the predicted stress drop, the upper axis in Figure 10 indicates the stress drop that would be associated with the plotted time for a few chosen W/L_b. To compare these predictions with our cycle simulation results, we assume $\dot{\theta}_m = 0.5$ and $V_c/V_0 = 100$ and calculate the stress drop at these intersections for a range of W/L_b. We plot the predicted stress drops along with the simulation results in Figure 7.

[70] These predictions reproduce several properties of the stress drops in the simulations. First, they match the decrease in stress drop with increasing W. The decrease arises because K_u increases with increasing along-dip length W while the negative contributions to K associated with friction do not. Thus events with larger along-dip lengths are able to propagate with smaller stress drops. The $K = 0$ analysis also correctly predicts that events are able to propagate with smaller stress drops in slip law simulations. This results from the smaller K_c associated with that evolution law. It predicts that the stress drops depend only weakly on V_c/V_0. This is consistent with the weak variation in the simulation results. Finally, the $K = 0$ analysis correctly predicts the preferred scaling of the simulation stress drops. As noted in section 5.2.2, both negative contributions to K (K_c and K_{mod}) scale roughly with $b\sigma\sqrt{L_b}$, and the positive contribution (K_u) scales with $\Delta\tau\sqrt{W}$. These scalings imply that a rough estimate of the stress drop is $\Delta\tau \approx \psi' b\sigma\sqrt{L_b/W}$, where ψ' is a constant that accounts for the geometric factor ψ and for the evolution-law-dependent scaling of $K_c + K_{\mathrm{mod}}$. Taking $\psi' = 20$ for the aging law and $\psi' = 7$ for the slip law reproduces the stress drops predicted by the $K = 0$ analysis to within 40% for W/L_b between 50 and 500,000, with the largest mismatch at the smallest W/L_b in this range.

[71] Each of the trends noted above can also be predicted by considering contributions to energy balance rather than contributions to K. As noted earlier, the dashed black curve in Figure 7 indicates the stress drop estimates from an energy balance approach, which is given by [*Hawthorne*, 2012]:

$$\Delta\tau \approx b\sigma \frac{1}{\psi''}\left(\frac{1}{2}\right)^{(2-n)/2}\left(\frac{W}{L_b}\right)^{-1/2} \left[\log\left(\frac{2V_c}{V_0}\right) + \log\left(\frac{W}{L_b}\right) + \log\left(\frac{\Delta\tau}{b\sigma}\right) + \log((1-\nu)\dot{\theta}_m)\right]^{n/2}. \quad (13)$$

Here ψ'' is a scaling factor of order 1 whose value was found empirically to be 0.4. Some properties of the stress drop predictions may be more intuitive in an energy balance context. For instance, the fracture energy scales with $b\sigma D_c$—with a local stress drop times a displacement—while the strain energy release rate scales with $W\Delta\tau^2/\mu$. Equating the two, we estimate that the stress drop scales with $b\sigma\sqrt{L_b/W}$, as observed in the simulations and predicted with the $K = 0$ approach.

[72] Both the $K = 0$ and the energy balance approaches thus predict the simulation stress drops relatively well. However, some of the variability in the stress drops shown in Figure 7 remains unexplained. In sections 5.3 and 5.4, we examine how that scatter arises.

5.3. Limitations from Nucleation

[73] As can be seen in Figure 7, some simulations have events with stress drops that are a few tens of percent larger than our $K = 0$ predictions. One slip law simulation even has events with stress drops twice as large. In this section we attempt to explain why such large-stress-drop events occur.

[74] In fact, these outliers are not the only simulation results that require further explanation. When making our stress drop predictions, we assumed a maximum velocity of $30V_{\tau\text{-min}}$. That seems appropriate given that slow slip events in cycle simulations exhibit such maximum velocities. However, the assumed slip rate is supposed to represent the minimum $V_{\max}$ that allows for steadily propagating events. In Appendix E, we show that it is possible to specify initial conditions such that steady propagation is possible for $V_{\max}$ between 5 and $15V_{\tau\text{-min}}$. Those artificially nucleated events have $|K_c + K_{\mathrm{mod}}|$, K_u, and stress drops that are 10% to 20% smaller than those plotted in Figure 7.

[75] Since the available stress drop increases roughly linearly with time in the inter-slow slip period, this implies that for most of the simulations plotted in Figure 7, an event that nucleated during the last 10% or 20% of the inter-slow slip period would have been able to rupture the entire fault. However, events nucleate only at discrete intervals. In most of the plotted simulations, two to seven events nucleate in each inter-slow slip period before one ruptures the entire fault. With this spacing of small events, lack of nucleation often delays the next major event by a few tens of percent. It causes a similar increase in the stress drops and K_u. Given the dependence of $|K_c + K_{\mathrm{mod}}|$ on maximum velocity shown in Figure 9, a few tens of percent increase in $|K_c + K_{\mathrm{mod}}|$ can cause the maximum velocity to increase from $10V_{\tau\text{-min}}$ to $40V_{\tau\text{-min}}$. Delayed nucleation thus seems capable of causing the factor of a few difference between the cycle simulation maximum velocities and the minimum allowable maximum velocities.

[76] In a few simulations, such as the slip law simulation with $W/L_b = 125$ marked by the open red diamond in Figure 7b, there are no small events between major slow slip episodes, and the stress drops are much larger than expected from the stress intensity factor approach. Such simulations seem like a rather poor representation of the slow slip events observed in Cascadia. Observations indicate that there are a number of bursts of tremor in the inter-slow slip period [e.g., *Wech and Creager*, 2011], and small but geodetically observable slow slip events accompany some of the bursts [e.g., *Wang et al.*, 2008]. To encourage the nucleation of small events, we include low-normal-stress regions and a sinusoidal forcing in many of our simulations (see sections 2 and 4.2). These complications introduce heterogeneity in

the slip rate during the inter-slow slip period. The value of the normal stress in the low-normal-stress region, the size of that region, and the amplitude of the sinusoidal forcing have only a minor influence on the stress drops, so long as several small slow slip events occur in each inter-slow slip period.

5.4. Heterogeneous Nucleation Resulting From Reaching Steady State

5.4.1. Description of Complicated Behavior

[77] This study focuses on simulations that exhibit periodic large slow slip events, as those are most easily compared with the observations. However, not all simulations display such a simple pattern of events. For instance, in the simulation shown in the second column of Figure 6, a few events rupture the entire fault, but most events extend less than $2W$ along strike, and it is sometimes difficult to identify the recurrence interval.

[78] Events that rupture only part of the fault are common in both periodic and complicated simulations. These failed events leave behind stress concentrations at their edge. It is only in complicated simulations, however, that new events nucleate at those stress concentrations. For instance, in Figure 6f, the events that begin at times 800, 1000, and 1600 nucleate near the center of the fault, at the locations of residual stress peaks.

[79] To understand why new events nucleate at leftover stress concentrations in some simulations but not in others, note that nucleation is possible only when a location is at or above steady state. In complicated simulations, the fault is often at steady state at the locations of leftover stress peaks. In simple periodic simulations, the fault is often below steady state even there, and if there is a region above steady state, it is quite small. The high stiffness implied by that small size inhibits acceleration.

5.4.2. Dependence on Model Parameters

[80] The fact that nucleation is possible only after the fault reaches steady state can help us understand why some simulations exhibit a complicated series of events and others do not. Specifically, more complicated behavior is favored by small along-dip lengths W/L_b and large a/b. Our goal is to predict when some location in the center of the fault would reach steady state as a result of the downdip loading. To do so, we use the approximations for the evolution of stress and state in the inter-slow slip period that we obtained in section 4.1. If we insert those approximations into equation (1), we can solve for the slip rate V, and thus obtain an approximation for $V\theta/D_c$ during the inter-slow slip period. We then ask when $V\theta/D_c$ will return to a value of 1—when the fault will reach steady state. These calculations provide an estimate of the time required to reach steady state, and of the stress accumulated during that time. The accumulated stress is approximately

$$\Delta\tau_{ss} \approx (b-a)\sigma \left[\log\left(\frac{2V_c}{V_0}\frac{b-a}{a}\right) + \log(\dot{\theta}_m) + \log\left(\frac{W}{L_b}\frac{b-a}{b}\frac{1}{1-\nu}\right) + \log\left(\frac{\Delta\tau}{(b-a)\sigma}\right)\right]. \quad (14)$$

We compute $\Delta\tau_{ss}$ for several a/b (and for $\dot{\theta}_m = 0.5$) and plot the results along with the stress drops in Figure 7 (dashed curves).

[81] More complicated behavior is expected if the fault reaches steady state before the stress drop becomes large enough to supply the fracture energy required for an event to rupture the entire fault. Consistent with this expectation, simulations exhibit complicated behavior and therefore do not have stress drops plotted in Figure 7 when the parameters imply a $\Delta\tau_{ss}$ that is smaller than our estimates of the stress drop required for propagation (when W/L_b plots to the left of the intersection of the concave-up and concave-down curves).

[82] The simulation behavior does not transition sharply from a simple periodic series of events to a chaotic series of events as we change a/b or W/L_b. In simulations with intermediate parameter values, there can be a series of events that rupture only a part of the fault, followed by a few events that rupture the entire fault. In these simulations, the stress drops in events that do rupture the entire fault are typically smaller than the $K = 0$ predictions. In Figure 7a, these low stress drops can be seen in the results for $a/b = 0.8$ and $W/L_b \leq 250$, and for $a/b = 0.9$ and $W/L_b \leq 500$.

6. Comparison With Observations

6.1. Propagation and Pattern of Events

[83] Slow slip events simulated with our chosen friction law and model geometry exhibit several features that are consistent with observations of slow slip in Cascadia and parts of Japan. The large events in our models propagate along strike at a steady rate, and they achieve along-strike lengths much longer than the along-dip length. Tremor observations indicate that large ETS (episodic tremor and slip) events propagate along strike at relatively steady rates of 5 to 15 km/day. They travel more than 200 km in Cascadia and more than 100 km beneath Shikoku and the Kii Peninsula. These distances are longer than the along-dip lengths, which are between 50 and 100 km in Cascadia and between 25 and 50 km in Japan [e.g., *Kao et al.*, 2006; *Wech et al.*, 2009; *Boyarko and Brudzinski*, 2010; *Obara*, 2010; *Creager et al.,*, 2011; *Houston et al.*, 2011; *Ide*, 2012]. Geodetic observations in both Cascadia and Japan have lower resolution but also indicate or are at least consistent with steady propagation on timescales of days [e.g., *Dragert et al.*, 2001; *Obara et al.*, 2004; *Hirose and Obara*, 2010; *Bartlow et al.*, 2011; *Dragert and Wang*, 2011].

[84] In steadily propagating events in the strip model, most of the slip accumulates in a region whose size depends on W. If the stress drop were perfectly uniform, 90% of the slip would accumulate within $0.5W$ of the front. In our cycle simulations, about 90% of the slip accumulates on the part of the fault near steady state—a region that extends up to 0.1 or $0.5W$ behind the front. Observations of large ETS events in Cascadia, Shikoku, and the Kii Peninsula indicate that at any given time, tremor is concentrated in a region that extends a few tens of kilometers along strike [e.g., *Kao et al.*, 2006; *Wech et al.*, 2009; *Boyarko and Brudzinski*, 2010; *Houston et al.*, 2011; *Obara*, 2010; *Ide*, 2012]. Given the along-dip lengths noted above, if regions with high tremor concentration can be interpreted as areas with rapid aseismic slip, such length scales seem consistent with the simulation results.

[85] Finally, many of the simulations produce a distribution of events that can easily be grouped into "large"

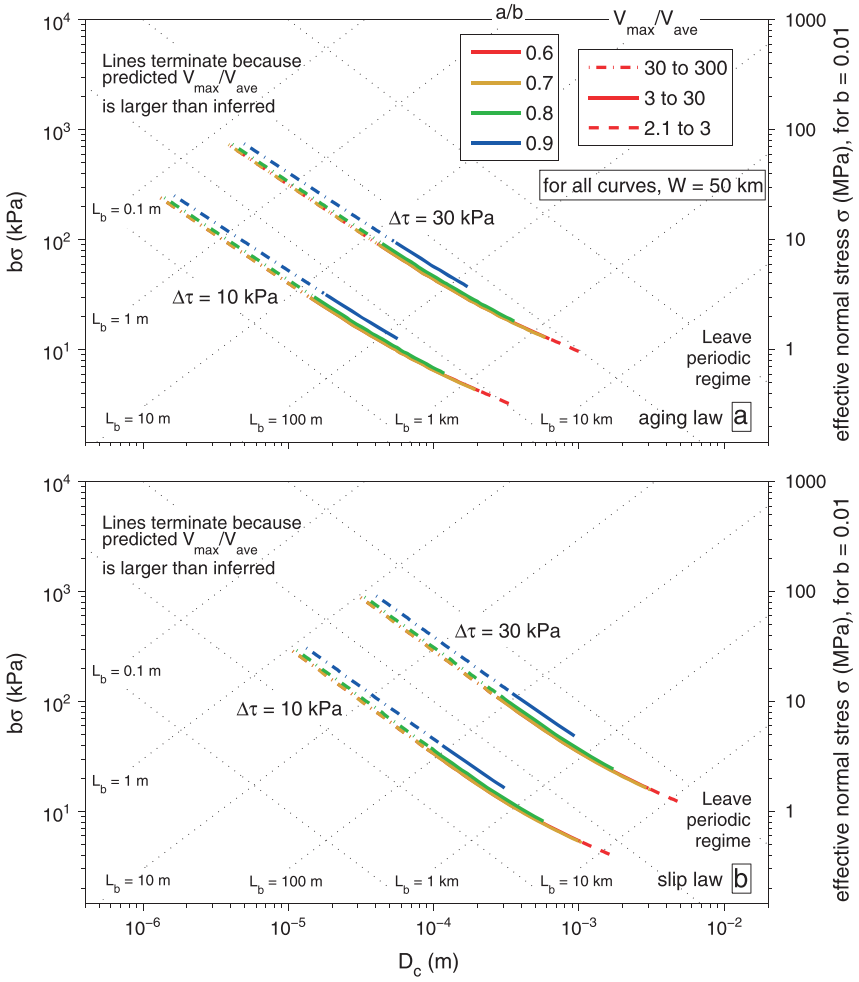

Figure 11. Colored curves: Combinations of $b\sigma$ and D_c that can match the stress drop observations using (a) the aging law and (b) the slip law. For all calculations, W is 50 km. The diagonal dotted lines with negative slope are contours of $b\sigma D_c$, with values of 0.1, 1, 10, and 100 Pa m, from bottom to top. The diagonal dotted lines with positive slope are contours of L_b. Color indicates a/b, and line style indicates the predicted V_{max}/V_{ave}. The V_{max}/V_{ave} that best matches the observations is around 10. We terminate the curves at the upper left when V_{max}/V_{ave} exceeds 300. We terminate the curves at the lower right when the simulations are expected to exhibit a complicated series of events rather than a set of periodic large events. A second constraint on the allowable values in the lower right comes from observations of localization of tremor, which suggests that L_b is at most a few kilometers for the aging law, and at most a few tens of kilometers for the slip law. These three constraints imply that this model can match the observations only if D_c is between about 1 μm and 2 mm. That range happens to be similar to values of D_c inferred from laboratory friction experiments, which typically fall between 1 and 100 μm [e.g., *Marone*, 1998].

and "small" events. This division is caused by the elongate fault geometry, which implies that the positive contribution to K scales with the stress drop times $\sqrt{W}$, not with the along-strike length L (equation (11)). The division is favored by larger along-dip lengths W/L_b and smaller a/b, as these parameters allow most of the fault to slip slowly and remain below steady state during the entire inter-slow slip period. The large simulated events occur at relatively regular intervals and can be compared with the 8, 14, and 22 month repeating events in Cascadia [e.g., *Dragert et al.*, 2001; *Brudzinski and Allen*, 2007; *Szeliga et al.*, 2008; *Wech et al.*, 2009; *Schmidt and Gao*, 2010]. The smaller simulated events can be compared with the tremor bursts and small slow slip events that occur in the inter-ETS period, which typically have sizes between 10 and 70 km [e.g., *Wang et al.*, 2008; *Wech et al.*, 2010; *Wech and Creager*, 2011]. In Shikoku and the Kii Peninsula, the large events might be compared with the tremor episodes that occur every 4 to 8 months, extend 100 to 150 km along strike, and are accompanied by geodetically observed slip. The small events might be compared with the more frequent tremor episodes that reach sizes up to 50 km but are not observed geodetically. However, the distinction between the large and small events is less striking in those regions than in Cascadia [e.g., *Obara et al.*, 2004; *Hirose and Obara*, 2010; *Ide*, 2010; *Obara*, 2010; *Sekine et al.*, 2010].

[86] The strip model parameterizes the stress as uniform in the dip direction, so it cannot reproduce the observation that many of the inter-ETS tremor bursts occur at the downdip edge of the slow slip region [e.g., *Obara*, 2010; *Wech and Creager*, 2011]. However, the continual perturbation of the fault by the steadily sliding downdip region may be adequately captured in our model by local loading due to the steadily sliding velocity-strengthening ($a > b$) section.

6.2. Stress Drops and Recurrence Intervals

[87] As noted in section 5.2, we can predict the stress drops in our simulations by requiring that the positive contribution to K associated with the stress drop be as large as the negative contribution associated with overcoming "static" friction. This equality can be approximated by $\Delta\tau\sqrt{W} \approx \psi' b\sigma\sqrt{L_b}$, where $\psi' \approx 20$ for the aging law and $\psi' \approx 7$ for the slip law (section 5.2.3). Here the left hand side is proportional to the positive contribution to K and is constrained by observations. Observations, therefore, also constrain the negative contribution to K and the combination of parameters $b\sigma\sqrt{L_b} = \sqrt{D_c\mu b\sigma}$. They do not, however, constrain the parameters individually.

[88] *Schmidt and Gao* [2010] estimated that the stress drops in Cascadia slow slip events are between 10 and 100 kPa, with a clustering around 30 kPa. We can also estimate the stress drop from the recurrence interval Δt, if we assume that the interface slips steadily downdip of the slow slip region and is locked updip. If the downdip slip rate V_0 is 10^{-9} m/s, or 3 cm/yr, an approximately 2 cm slip deficit accumulates in the center of the slow slip region during each 12 to 16 month recurrence interval. The stress drop in an event $\Delta\tau$ is roughly $\mu(1-\nu)^{-1}/W$ times that slip deficit, or $(\Delta t V_0/2)\mu(1-\nu)^{-1}/W$ (see section 5.2.1). If the along-dip extent W is 50 km [e.g., *Szeliga et al.*, 2008; *Wech et al.*, 2009; *Schmidt and Gao*, 2010], the shear modulus μ is 30 GPa, and Poisson's ratio ν is 0.25, 2 cm of slip implies a stress drop around 15 kPa. With this same equation, we can estimate the recurrence interval Δt that corresponds to a specified stress drop. Thus, if the model can match the geodetically inferred stress drops with values of W, μ, and V_0 that satisfy the observations, it can also match the observed recurrence intervals.

[89] When we insert plausible stress drops into $\Delta\tau\sqrt{W} \approx \psi' b\sigma\sqrt{L_b}$, we find that if the shear modulus is 30 GPa, the stress drop is between 10 and 50 kPa, and W is between 50 and 100 km, for our model to match the observations, $D_c b\sigma$ must be between 0.3 and 20 Pa m for the aging law and between 3 and 200 Pa m for the slip law. We illustrate the trade-off between $b\sigma$ and D_c in Figure 11, where we use the full $K = 0$ stress drop predictions from section 5.2 to calculate the $b\sigma$ required to match the observed stress drops as a function of the assumed D_c. For that figure we assume that W is 50 km and that $\dot{\theta}_m$ is 0.5.

[90] We should note that the stress drop predictions used to make Figure 11 assume that the slip rate decays behind the front as described in section 3.2.2 and that the final stress in each event is close to the minimum steady state stress $\tau_{\text{ss-min}}$. We have verified those assumptions only in the simulations we have run, which have W/L_b less than 1000. It is possible that these assumptions require modification when we extrapolate the stress drops to W/L_b several orders of magnitude larger than 1000—to L_b much smaller than 50 m in Figure 11. For example, if most of the slip accumulates over a distance much less than W when W/L_b is large, the stress well behind the front could increase to values significantly larger than $\tau_{\text{ss-min}}$.

[91] The curves in Figure 11 terminate at both small and large L_b for reasons that will be discussed in sections 6.3 and 6.4. With these terminations and a laboratory value of b of 0.01 [e.g., *Marone*, 1998], allowable effective normal stresses range from about 0.1 to 100 MPa for both the aging and slip laws. Much of this range of normal stress is small compared to the stress due to the overburden, which is around 1 GPa in the slow slip region. Seismic imaging suggests that such low effective normal stresses might be explained by high pore pressure [e.g., *Kodaira et al.*, 2004; *Audet et al.*, 2009; *Matsubara et al.*, 2009; *Peacock et al.*, 2011]. The larger normal stresses that fit the observed stress drop may be too large to allow for the response of tremor and slow slip to 1-kPa-amplitude tidal forcing [*Rubinstein et al.*, 2008; *Lambert et al.*, 2009; *Hawthorne and Rubin*, 2010]. In the companion paper, we show that it is difficult to find a set of parameters that allows our model to simultaneously match the observed tidal modulation and stress drops. If the normal stress relevant for slow slip is also relevant for tremor, the larger normal stresses may also make it difficult to match the observed dynamic triggering of tremor by 10-kPa-amplitude seismic waves [*Rubinstein et al.*, 2007, 2009; *Gomberg*, 2010].

6.3. Upper Bound on L_b and D_c

[92] The observed stress drops and W are not the only constraints on the model parameters. Two additional features set an upper bound on L_b. As discussed in section 5.4, if W/L_b is too small, simulations exhibit complicated behavior rather than quasi-periodic events that rupture the entire fault. In Figure 11, we terminate the curves at the lower right when W/L_b gets too small to allow for large periodic events.

[93] In rate and state simulations, rapid slip rates localize on a length scale of L_b for the aging law and $L_b b\sigma/\Delta\tau_{\text{p-r}}$ for the slip law [e.g., *Dieterich*, 1992; *Rubin and Ampuero*, 2005; *Ampuero and Rubin*, 2008]. We do not see variations in slip rate on much shorter length scales. Observations indicate that tremor concentration varies behind the front on length scales shorter than 10 km, and the widths of tremor streaks are often less than 10 km [e.g., *Ghosh et al.*, 2010a, 2010b]. If localization of tremor implies a localization of high slip rates, this suggests that in Cascadia, L_b should be at most several kilometers for the aging law and at most several tens of kilometers for the slip law. It implies that parameters in the lower right corner of Figure 11 do not allow for simulations that match the observations.

[94] These constraints imply that for our model to match the observations, D_c must be smaller than about 3 mm (Figure 11). If $b = 0.01$, they imply that σ is larger than about 0.2 MPa for the aging law and larger than about 0.5 MPa for the slip law.

6.4. Average Slip and Propagation Rates

[95] In slow slip events in Cascadia, slip rates are of order 1 cm/day, or 10^{-7} m/s [e.g., *Dragert et al.*, 2001; *Bartlow et al.*, 2011; *Dragert and Wang*, 2011], and along-strike propagation rates are around 10 km/day, or 10^{-1} m/s

[e.g., *Wech et al.*, 2009; *Bartlow et al.*, 2011; *Dragert and Wang*, 2011]. In our simulations, the slip rates are controlled by the minimum steady state stress velocity $V_{\tau\text{-min}} = V_c(b - a)/a$ (equation (5)). We can tune the cutoff velocity V_c to match the slip rates in the observed events. This tuning does not change the match with the observed stress drops because the modeled stress drops depend negligibly on the cutoff velocity (see section 5.2.3).

[96] If we tune the simulations to exhibit the observed slip rates and stress drops, they will automatically exhibit the observed propagation rates V_{prop}. To see this, we define V_{ave} as the mean slip rate within W of the front and δ as the maximum slip in the event. Then from elasticity, $V_{\text{prop}} \approx V_{\text{ave}} W/\delta \approx V_{\text{ave}}\mu(1-\nu)^{-1}/\Delta\tau$.

[97] This is not the only constraint on V_{prop}, however. In the simulations, $V_{\text{prop}} \approx \alpha V_{\text{max}}\mu/\Delta\tau_{\text{p-r}}$ (equation (7)) because of properties of the near-tip region. Equating the two expressions for V_{prop} determines a relationship between the maximum velocity V_{max} and the average slip rate V_{ave}: $V_{\text{max}}/V_{\text{ave}} \approx \alpha^{-1}(1-\nu)^{-1}\Delta\tau_{\text{p-r}}/\Delta\tau$. Here the peak to residual stress drop $\Delta\tau_{\text{p-r}}$ is approximately $b\sigma\,[\log(V_c\theta_i/2D_c + 1) - \log(2V_c/V_{\text{max}} + 1)]$ (equation (6)). It is of order $10b\sigma$ for the part of parameter space shown in Figure 11.

[98] With these considerations, we can predict a $V_{\text{max}}/V_{\text{ave}}$ for each point on the curves in Figure 11. In the simulations we have run, $V_{\text{max}}/V_{\text{ave}}$ is of order 10. Such a value seems consistent with the geodetic inferences that the slip rate decays on length scales comparable to W [e.g., *Dragert and Wang*, 2011], and seismic observations that tremor persists several tens of kilometers behind the front [e.g., *Wech and Creager*, 2008; *Ghosh et al.*, 2010a]. In the simulations, most of the slip accumulates in the region near steady state, at slip rates between $V_{\tau\text{-min}}$ and V_{max} (see section 3.2.2). As long as this region spans a significant fraction of W, V_{ave} should not be much smaller than $V_{\tau\text{-min}}$. V_{max} is unlikely to be much more than $40V_{\tau\text{-min}}$ because K_{mod}, one of the negative contributions to K, increases strongly with $V_{\text{max}}/V_{\tau\text{-min}}$. It thus seems unlikely that $V_{\text{max}}/V_{\text{ave}}$ is many orders of magnitude different from 10.

[99] In Figure 11, we indicate the $V_{\text{max}}/V_{\text{ave}}$ implied by the model parameters with the line style. We terminate the curves in the upper left corner of Figure 11 when $V_{\text{max}}/V_{\text{ave}}$ exceeds 300. Those terminations imply an upper bound on $b\sigma$ of about 1 MPa. They imply a lower bound on D_c of about 1 μm for the aging law and about 10 μm for the slip law.

6.5. Variations in Slip and Propagation Rates

[100] According to the $K = 0$ requirement, the maximum velocity in a propagating event should increase if the available stress drop or the along-dip length W increases. However, because the chosen friction law is steady state velocity strengthening at high slip rates, V_{max} varies by only a factor of a few with tens of percent variations in the stress drop and W. This contrasts with the stronger exponential dependence of V_{max} on these parameters that is seen with standard velocity-weakening rate and state friction [e.g., *Rubin and Ampuero*, 2005; *Ampuero and Rubin*, 2008]. The propagation rate V_{prop} is proportional to V_{max} (equation (7)) and thus varies by a similar amount. Such a small variation in propagation rate seems consistent with observations, as the propagation rate of tremor often varies only by a factor of a few on timescales longer than one day [e.g., *Kao et al.*, 2006; *Wech and Creager*, 2008; *Boyarko and Brudzinski*, 2010; *Houston et al.*, 2011], and tremor and slow slip are plausibly colocated [e.g., *Dragert et al.*, 2001; *Obara et al.*, 2004; *Hirose and Obara*, 2010; *Bartlow et al.*, 2011; *Dragert and Wang*, 2011]. Further, the slip and propagation rates in a given subduction zone segment vary from event to event by a similar amount despite tens of percent differences in the interevent time. Finally, W and $\Delta\tau$ might vary even more between Cascadia and Japan, but the propagation speeds are quite similar [e.g., *Dragert et al.*, 2001; *Obara et al.*, 2004; *Kao et al.*, 2006; *Wech and Creager*, 2008; *Boyarko and Brudzinski*, 2010; *Hirose and Obara*, 2010; *Bartlow et al.*, 2011; *Dragert and Wang*, 2011].

7. Conclusions

[101] We have examined a number of properties of slow slip events simulated with a steady state velocity-weakening to velocity-strengthening friction law in a strip model geometry. The geometry allows steady propagation of large events and dictates that slip accumulates in a region whose size is somewhat smaller than the along-dip extent W. It also provides a framework for understanding the stress drops and recurrence intervals of large events. In our simulations, a number of events nucleate in a small region that is loaded by a steadily sliding section with $a > b$. Most of these events fail before propagating a distance W, but events do rupture the entire fault periodically in many simulations. The stress drop $\Delta\tau$ in those larger events can be determined by considering a balance between the positive contributions to the stress intensity factor K associated with the stress drop and the negative contributions associated with frictional dissipation. The corresponding recurrence interval Δt is approximately $2W(1-\nu)\Delta\tau/\mu V_0$. The stress drops in large events are given roughly by $\psi' b\sigma\sqrt{L_b/W}$, where $\psi' = 20$ for the aging law and $\psi' = 7$ for the slip law. They scale with $\sqrt{b\sigma D_c}$ because that parameter set determines the negative contributions to K. They are smaller in slip law simulations because the negative contribution K_c is smaller for the slip law. Finally, they decrease with increasing along-dip length W because the positive contribution to K scales with $\sqrt{W}$ but the negative contributions are independent of it.

[102] We also use the stress intensity factor requirement to understand the slip and propagation rates in our simulations. In both this and the stress drop analysis, we must account for the gradual decay of stress behind the propagating front. That decay occurs along the steady state stress-velocity curve. It arises because of the velocity-strengthening character of the chosen friction law at high slip rates, and it causes the slip and propagation rates to vary weakly with the stress drop and W.

[103] The modeled events exhibit several features consistent with observations of slow slip and tremor. These include steady propagation, an appropriate length scale for accumulation of slip, a pattern of large and small events, and relatively small variations in propagation rates. The observed slip rates can be matched by tuning the cutoff velocity, and it is possible to choose the remaining parameters to match the observed propagation rates and stress drops. Together, these three observations set a lower bound on D_c

of 1 to 10 μm and an upper bound on $b\sigma$ of about 1000 kPa. The requirement that large events occur episodically sets an upper bound on D_c of about 3 mm and a lower bound on $b\sigma$ of about 1 kPa. For laboratory values of b (0.01), the effective normal stress σ should be 0.1 to 100 MPa. This upper bound is higher than is typically invoked in models of slow slip, and it may be too large to permit the modulation of slow slip and tremor by the tides or passing surface waves. However, using the adopted friction law, low effective stress is not required to produce episodic slow slip events with the observed stress drops and propagation speeds.

[104] Laboratory values of D_c are typically between 1 and 100 μm [e.g., *Marone*, 1998], within the range of D_c inferred here. The D_c values here are mostly similar to or smaller than those inferred from postseismic and interseismic slip, which are between 100 μm and several mm [e.g., *Fukuda et al.*, 2009; *Kanu and Johnson*, 2011]. They are mostly smaller than those inferred from earthquake slip models, which can be centimeters to meters [e.g., *Ide and Takeo*, 1997; *Bouchon et al.*, 1998; *Guatteri et al.*, 2001; *Fletcher and McGarr*, 2006]. That is expected, as D_c should be considerably smaller than the total slip in each ETS event, which is just a few centimeters. Also, the D_c estimates from earthquakes are upper bounds, and they may be related to the effects of additional weakening mechanisms that operate at high slip speeds.

[105] Models with other friction laws can also reproduce the observed slip velocities, propagation rates, and recurrence intervals [*Liu and Rice*, 2005, 2007; *Rubin*, 2008; *Liu and Rubin*, 2010; *Segall et al.*, 2010; *Skarbek et al.*, 2012]. It seems likely that they could also match the along-strike propagation in the strip model geometry. Distinguishing between these models will require attempting to reproduce other observed features of slow slip, such as tidal modulation and back-propagating fronts. We carry out such a comparison in the companion paper.

Appendix A: Strip Model Details

A1. Relationship Between Slip and Stress

[106] As described in section 2.2, we wish to determine the relationship between stress and slip along the central (along-strike) line of the rectangular slow slip region, assuming that the stress within that region is uniform along dip (see Figure 2). Because of the symmetry in the chosen geometry, this relationship can be simply constructed in the wavenumber domain. We define

$$\hat{\delta}(k) = \frac{1}{L}\int_{-L/2}^{L/2} \delta(x) e^{ikx} \mathrm{d}x \tag{A1}$$

$$\hat{\tau}_{el}(k) = \frac{1}{L}\int_{-L/2}^{L/2} \tau_{\mathrm{el}}(x) e^{ikx} \mathrm{d}x \tag{A2}$$

where δ is slip (in the dip direction) along the central line, τ_{el} is the corresponding stress, L is the along-strike fault length, x is the distance along-strike, and k is the wavenumber (2π/wavelength) in the along-strike direction. For the moment, we consider only $k \neq 0$. Stress and slip are related according to

$$\hat{\tau}_{el}(k) = \hat{\delta}(k) K_s(k), \tag{A3}$$

where $K_s(k)$ is the stiffness at wavenumber k. To obtain each $K_s(k)$, we numerically determine the full 2-D fault (3-D elasticity) solution in which slip is zero outside of the modeled slow slip region, and in which stress varies sinusoidally with wavenumber k in the along-strike direction but is uniform along dip within the slow slip region. In the long wavelength limit ($k^{-1} \gg W$), where slip and stress are nearly uniform along strike, $K_s(k)$ tends to $\mu(1-\nu)^{-1}/W$. This is the solution for a mode-II crack of infinite length along strike and length W in the dip direction. For along-strike variations on length scales much shorter than W ($k^{-1} \ll W$), $K_s(k)$ tends to $\mu/2k$. This is the solution for a one-dimensional (line) fault subjected to slip in the orthogonal direction. Our numerical calculations of $K_s(k)$ reproduce the short-wavelength limit almost exactly and the long wavelength limit to within 0.5%.

[107] When we consider the relationship between the average slip and stress on the fault (the $k = 0$ case), we must also include the effect of slip downdip of the modeled strip. For a downdip slip rate of V_0 and an updip slip rate of zero, the $k = 0$ elasticity equation is

$$\hat{\tau}_{el}(0) = \frac{\mu}{(1-\nu)W}\left(\frac{V_0 t}{2} - \hat{\delta}(0)\right). \tag{A4}$$

where t is the time since the beginning of the simulation.

A2. Calculating Contributions to K

[108] As noted in section 5.2.1, the stress intensity factor K is given by

$$K = \int_0^{L_s} c_k(x)(\tau_{\mathrm{init}} - \tau(x))\mathrm{d}x, \tag{A5}$$

where x is distance behind the front and the coefficients $c_k(x)$ depend on the model geometry and on L_s. To determine the c_k for a given x in our geometry, we define x' as the distance behind the front, and we numerically find the slip and stress profile along the center line that has zero slip ahead of the tip ($x' < 0$), zero slip well behind the front ($x' > 4W$), a specified nonzero stress τ_{spec} in the cell at $x' = x$, and zero stress at all other locations within $0 < x' < 4W$. If K is the stress intensity factor associated with that solution, the slip profile $\delta(x')$ just behind the tip is given by $K\sqrt{(x')}$ [e.g., *Lawn*, 1993]. We estimate this K from the numerically determined slip profile. The coefficient $c_k(x)$ is then K/τ_{spec} divided by the cell size.

[109] In these calculations, each cell spans at most $10^{-4}W$ along strike. For $x > 0.01W$, reducing the cell size further changes $c_k(x)$ by less than a few percent. However, the numerical accuracy breaks down closer to the tip. To better estimate c_k in that regime, we recall that such short-wavelength variations in stress do not depend on the along-dip length W. For $x < 0.01W$, we assume that $c_k(x)$ is $(2/\pi x)^{1/2}$, the coefficient appropriate for an antiplane strain model [e.g., *Lawn*, 1993; *Tada et al.*, 2000, p. 87]. The numerically calculated $c_k(x)$ follow $(2/\pi x)^{1/2}$ to within a few percent for $.005W < x < 0.02W$.

[110] $c_k(x)$ decays with distance behind the front, and in the simulations the contributions to K are negligible for $x > 2W$. When calculating c_k for $x < 2W$, the along-strike length of the region with nonzero slip L_s is relatively unimportant. The $c_k(x)$ change by less than a few percent when L_s is changed from $4W$ to $3W$.

[111] If we wish to know the stress intensity factor associated with a stress drop that is uniform behind the front, we can insert that stress drop into equation (A5) and integrate

with the numerically calculated $c_k(x)$. Alternatively, we can numerically determine the slip and stress that follow the strip model elasticity and have zero slip for $x < 0$ and $x > 4W$ and some specified uniform stress drop $\Delta\tau_{\text{spec}}$ for $0 < x < 4W$, and then determine K from the near-tip slip profile. Both calculations imply that $K = \psi\Delta\tau_{\text{spec}}\sqrt{W}$. The former calculation gives $\psi = 0.90$, while the latter gives $\psi = 0.87$. The few percent discrepancy seems acceptable given the accuracy of the c_k calculations and how they are used in this work.

Appendix B: Estimating K_c

B1. Near-Tip Stresses Dictated by the Friction Law

[112] In order to estimate K_c, we need to know the stress in the near-tip region. We can estimate these stresses analytically by using the friction law because, in this region, state is changing quickly while velocity is changing slowly. If we assume the slip rate is constant, and if we define τ_{ref} as the steady state stress for that slip rate, stress evolves with displacement as

$$\tau(\delta) - \tau_{\text{ref}} \approx \Delta\tau_{\text{p-r}} - \frac{b\sigma}{D_c}\delta \tag{B1}$$

for the aging law and

$$\tau(\delta) - \tau_{\text{ref}} \approx \Delta\tau_{\text{p-r}} e^{-\delta/D_c} \tag{B2}$$

for the slip law. Here $\Delta\tau_{\text{p-r}}$ is the maximum stress minus τ_{ref}, as introduced in section 3.2.1. Equation (B1) also uses the approximation that $V_{\max}\theta_i/D_c \gg 1$. These expressions for the change in stress are identical to those obtained for standard rate and state friction [e.g., *Bizzarri and Cocco*, 2003; *Ampuero and Rubin*, 2008].

[113] In reality the slip rate is not quite uniform in the near-tip region. In almost all of the simulations presented in Appendix E, it is 2 to 2.5 times smaller than the maximum velocity $V_{\max}$ and increasing at the time of the maximum stress, and it falls to about $V_{\max}/2$ by the time the fault reaches steady state. We therefore take $\tau_{\text{ref}} = \tau_{\text{ss}}(V_{\max}/2)$, equal to the steady state stress at $V_{\max}/2$. To complete our approximations, we note that by the time of the maximum stress, state has evolved from its initial value θ_i to about $\theta_i/2$. This implies a peak to residual stress drop of

$$\Delta\tau_{\text{p-r}} \approx b\sigma\left[\log\left(\frac{V_c\theta_i}{2D_c} + 1\right) - \log\left(\frac{2V_c}{V_{\max}} + 1\right)\right]. \tag{B3}$$

This estimate matches the actual peak to residual stress drop to within 5% for almost all of the aging law simulations and most of the slip law simulations presented in Appendix E. It matches the simulations to within about 10% if the two empirical factors of 2 in the terms $V_c\theta_i/2D_c$ and $2V_c/V_{\max}$ are dropped.

B2. Analytical Integration

[114] To estimate K_c, we take the contributing stress change profile $\Delta\tau_c$ to be $\tau(\delta) - \tau_{\text{ref}}$ from equations (B1) and (B2). We wish to insert this expression into equation (8) and integrate within the near-tip region. For this calculation, we assume that the tip is at the location of the maximum stress. Because the region of interest is very close to the tip relative to W, it is sufficient to use the coefficients $c_k(x)$ for an antiplane strain model, and [e.g., *Lawn*, 1993; *Tada et al.*, 2000, p. 87]:

$$K_c = \sqrt{\frac{2}{\pi}}\int_0^R \frac{\Delta\tau_c(x)}{\sqrt{x}}\mathrm{d}x. \tag{B4}$$

Here R is the size of the slip-weakening region that contributes to K_c.

[115] The friction law provides $\Delta\tau_c$ as a function of displacement δ, not distance x. To rewrite equation (B4) in terms of displacement, we assume a uniform slip rate in the near-tip region. This leads to $\delta(x) = \alpha x$. The constant α accounts for the shape of the local stress profile. It is the same α as that in the $V_{\text{prop}} - V_{\max}$ relation in equation (7). Equation (B4) now becomes

$$K_c \approx \sqrt{\frac{2\alpha}{\pi}}\sqrt{\frac{\mu}{\Delta\tau_{\text{p-r}}}}\int_0^{\delta_{\max}} \frac{\Delta\tau_c(\delta)}{\sqrt{\delta}}\mathrm{d}\delta. \tag{B5}$$

[116] For the aging law, this approximation predicts that the fault reaches steady state after a slip of $D_c\Delta\tau_{\text{p-r}}/b\sigma$, so we use this value as our maximum slip $\delta_{\max}$. For the slip law, it is less clear what value to use for $\delta_{\max}$. However, most of the contribution to K comes from the high-stress and low-slip part of this curve, which is near the tip, so the exact choice of $\delta_{\max}$ does not strongly affect the result. We find that taking $\delta_{\max} = \infty$ provides a reasonable approximation of the integral in equation (B5).

[117] Inserting equations (B1) and (B2) into equation (B5) and evaluating, we obtain

$$K_c \approx \frac{4}{3}\sqrt{\frac{2\alpha}{\pi}}\Delta\tau_{\text{p-r}}\sqrt{\frac{D_c\mu}{b\sigma}} \tag{B6}$$

for the aging law and

$$K_c \approx \sqrt{2\alpha\mu D_c\Delta\tau_{\text{p-r}}} \tag{B7}$$

for the slip law. The peak to residual stress drop $\Delta\tau_{\text{p-r}}$ can be estimated as a function of the maximum velocity and initial state, as in equation (6).

B3. Scaling to Numerical Estimates

[118] When we obtained the analytical estimates of K_c (equations (B6) and (B7)), we made several assumptions that are not quite accurate. The most problematic of these is the assumption that the tip of the propagating front is at the location of peak stress. When using the $K = 0$ criterion, we should define the tip as a point separating the region with finite slip from the region ahead of the front with essentially zero slip in this event. It is straightforward to visually identify such a location on a plot of log of displacement versus distance. For most of the simulations in Appendix E, the tip is $0.25L_b$ ahead of the maximum stress when using the aging law and $0.03L_b$ ahead of the peak stress when using the slip law. That distance does not vary systematically with $V_{\max}$ or other model parameters.

[119] To examine the error in our K_c estimates, we numerically calculate K_c using the correct tip and divide by the analytical estimates of equations (B6) and (B7). The resulting ratios are around 1.4 for the aging law and 1.2 for the slip law. The ratios vary by only a few percent for the aging law and by 10% to 20% for the slip law among

the steadily propagating simulations in Appendix E, and there is no systematic variation with the maximum velocity or stress drop. Given this consistency, for a final approximation of K_c, we retain the form of the analytical estimates but allow a constant scaling:

$$K_c = \beta \sqrt{D_c b\sigma\mu \left[\log\left(\frac{V_c\theta_i}{2D_c} + 1\right) - \log\left(\frac{2V_c}{V_{\max}} + 1\right)\right]^{n-1}}. \quad \text{(B8)}$$

We use a scaling constant β of 1.1 for the aging law and 1.3 for the slip law.

Appendix C: Empirical Fits to Stress and Slip Rate in the Region Near Steady State

[120] To know precisely how slip rate and stress decay behind the front, we must solve the full elasticity and friction equations. We are unable to come up with a simple approximation to the velocity and stress within the entire region near steady state. However, if we consider only the portion of this region within $0.1W$ of the tip, we find that the slip rate falls off as $x^{-1/2}$, where x is the distance behind the front. This is the same slip rate profile characteristic of propagating uniform stress drop events.

[121] Since the fault is near steady state in this region, the stress can be written as a function of the slip rate. If $d\tau_{ss}/d\log V$ is roughly constant, a velocity that decays as $x^{-1/2}$ implies a stress that decreases linearly with $\log(x)$. This is indeed the case in many simulations. Figure C1 shows a few typical examples of velocity, stress, and $V\theta/D_c$ profiles. These are taken from the steadily propagating simulations described in Appendix E.

[122] This simple scaling of velocity and stress breaks down very near the tip, where the fault is above steady state and stress is changing quickly. We find that it is a reasonable approximation to assume that the fault is near steady state and that the slip rate decays as $x^{-1/2}$ starting a distance $0.9L_b$ behind the tip in aging law simulations and starting a distance $2.5L_b(b\sigma/\Delta\tau_{p\text{-}r})$ behind the tip in slip law simulations. The open circles on the curves in Figure C1c are plotted at these distances. The velocity at these locations is around $0.6V_{\max}$ in aging law simulations and $0.5V_{\max}$ in slip law simulations.

[123] We plot profiles with these reference velocities and with a scaling of $x^{-1/2}$ in Figure C1a (dashed lines). The dashed lines in Figure C1b indicate the stress profiles implied by those velocities, assuming $V\theta/D_c = 1$. The predicted velocity and stress profiles reasonably match the simulated ones within about $0.1W$ of the front.

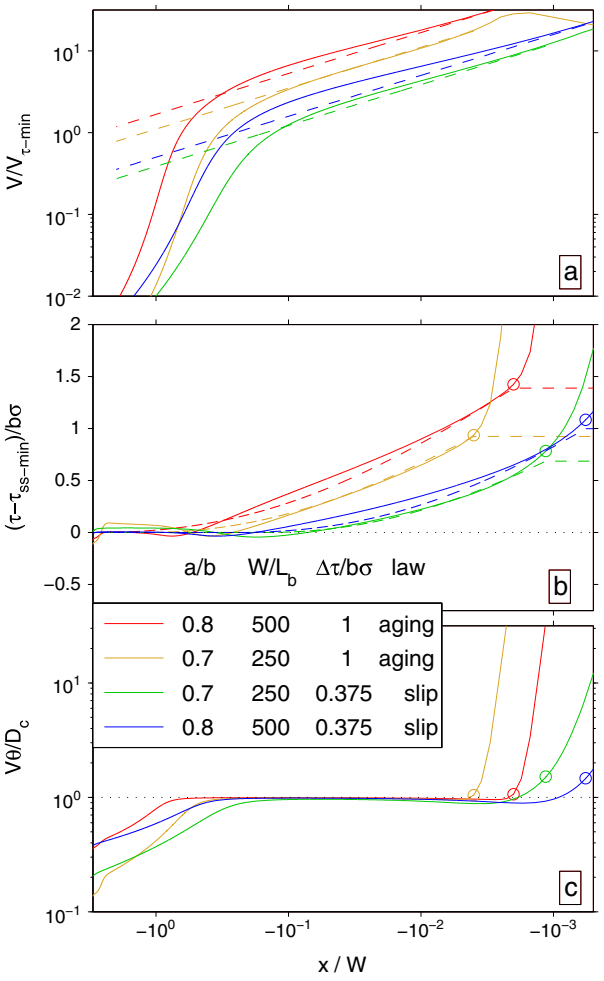

Figure C1. Solid curves: Profiles of (a) velocity, (b) stress, and (c) $V\theta/D_c$ during several steadily propagating simulations. In Figure C1a, the dashed lines indicate our approximation for slip rate, which has $V \sim x^{-1/2}$. The dashed lines in Figure C1b indicate the steady state stress implied by the approximations for velocity shown in Figure C1a. The circles in Figures C1b and C1c indicate the location where we assume the fault reaches steady state.

Appendix D: Details of K_{mod} Calculations

[124] In order to estimate K_{mod} as a function of V_{max} and θ_i, we use the empirical approximations to stress behind the front obtained in Appendix C. We assume that the stress change profile $\Delta\tau_{mod}$ is the difference between those empirical estimates and the minimum steady state stress $\tau_{ss\text{-}min}$. Since calculations of K strongly weight the changes in stress close to the tip, it is acceptable that the empirical approximations for stress are accurate only up to $0.1W$ behind the front.

[125] The approximations for stress behind the front are made for regions near steady state. They begin either $0.6L_b$ or $2.5L_b b\sigma/\Delta\tau_{p\text{-}r}$ behind the location of maximum stress for the aging law or the slip law, respectively. Closer to the front, we take the $\Delta\tau_{mod}$ to be $\tau_{ss}(0.6V_{max}) - \tau_{ss\text{-}min}$ for the aging law and $\tau_{ss}(0.5V_{max}) - \tau_{ss\text{-}min}$ for the slip law. That stress supplements the contributions to K from K_c and K_u from this region, so that the three stress change profiles sum to the actual stress change profile. In fact, we extend this assumed stress either $0.25L_b$ (aging law) or $0.03L_b$ (slip law) ahead of the modeled location of maximum stress, to account for the fact that the tip is slightly ahead of the maximum stress (Appendix B3). That extension modifies the calculated K_{mod} by at most a few percent.

[126] The estimated $K_{mod} + K_c$ is plotted as a function of V_{max} in Figure 9. K_{mod} is near zero for maximum velocities not much larger than $V_{\tau\text{-}min}$ and increases with increasing slip rate, since higher slip rates imply larger stresses in the region near steady state. It depends more strongly on V_{max}

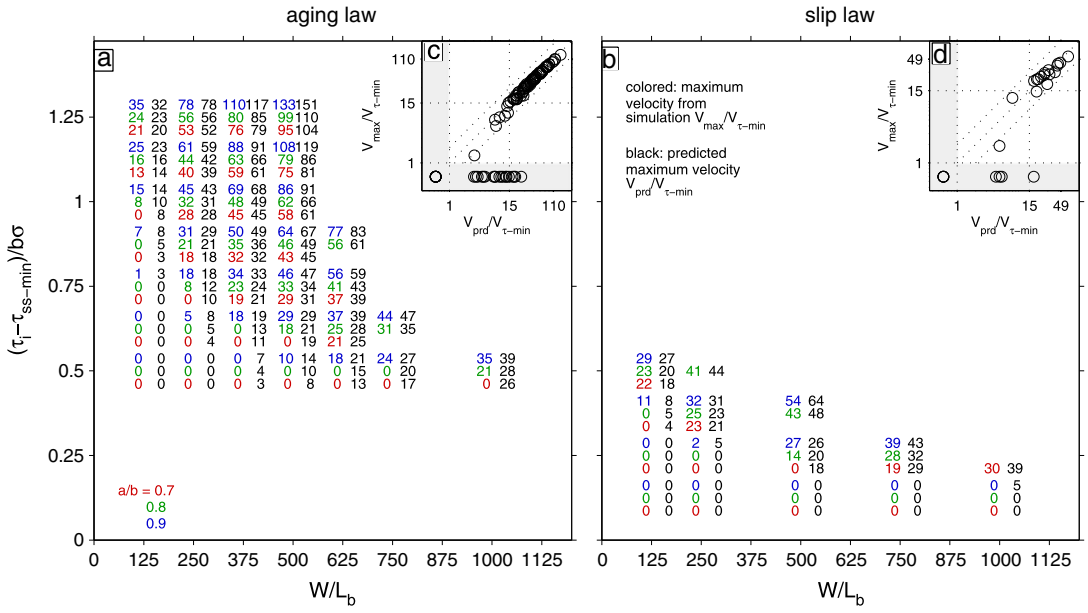

Figure E1. Observed (colored) and predicted (black) maximum velocities in a number of steadily propagating simulations for (a) the aging law and (b) the slip law. Vertical location indicates the initial stress relative to $\tau_{ss\text{-}min}$ and color indicates a/b. Each set of six values is for simulations with a single value of initial stress and W/L_b, as indicated by the location of the center of the cluster. Values of zero indicate that the event did not propagate (colored zeros) or was predicted to not propagate (black zeros). The inset axes (c and d) are plots of the observed versus the predicted maximum velocities. Most values plot within the outer diagonal dotted lines, which indicate over- and under-predictions of a factor of 2. Events that are observed or predicted not to propagate are plotted in the horizontal or vertical gray bars, respectively.

when V_{max} is larger because the steady state stress varies more quickly with slip rate in that case, and changes in V_{max} cause larger changes in stress behind the front. At slip rates larger than $10V_{\tau\text{-min}}$, the dependence of K_{mod} on V_{max} is much stronger than the logarithmic dependence of K_c on V_{max} typical of a standard velocity-weakening friction law [e.g., *Rubin and Ampuero*, 2005; 2008, *Ampuero and Rubin*].

[127] For the aging law, K_{mod} depends only on V_{max} and the model parameters. It does not depend on the value of state ahead of the propagating front θ_i. For the slip law, K_{mod} is actually smaller for larger initial state θ_i because the size of the region above steady state is smaller, and stress begins to decay closer to the front. However, this dependence on θ_i is weak; $|K_c + K_{mod}|$ always increases with θ_i because $|K_c|$ increases with θ_i.

[128] K_{mod} depends only weakly on the parameters W and a/b. It depends weakly on W because the empirical stress profiles from Appendix C do not depend on W, and because most of K_{mod} is accumulated close to the front relative to W. In this region, the weights $c_k(x)$ for calculating K from the stress change (equation (9)) are similar for the strip model and for 2-D elasticity. K_{mod} depends weakly on a/b because $\tau_{ss}(V_{max})-\tau_{ss\text{-}min}$ depends only weakly on a/b when written as a function of $V_{max}/V_{\tau\text{-min}}$. K_{mod} is slightly smaller for larger a/b, as seen in Figure 9. This effect results in the slightly smaller stress drop predictions for large a/b in section 5.2. It can also account for the increase in $V_{max}/V_{\tau\text{-min}}$ with a/b among events with identical initial conditions, as seen in Figure E1.

Appendix E: Testing Estimates of K Contributions by Comparison With Steadily Propagating Simulations

E1. Steadily Propagating Simulations

[129] We can compare our estimates of the contributions to K to the actual values extracted from events in cycle simulations. However, in those simulations there is often some heterogeneity in the initial stress that makes such a comparison imprecise, and the range of velocities seen in cycle simulation events is limited. To avoid complications and to examine a broader range of maximum velocities, we design a set of simulations that rupture a region with uniform initial stress and state. We consider faults with length between 4 and $8W$ that are bounded on both along-strike ends by regions that are forced to slip at rates many orders of magnitude below V_c. These faults are governed by strip model elasticity, but the downdip loading rate is effectively zero. At the beginning of each simulation, the stress everywhere is given a specified value that is larger than the minimum steady state stress. On most of the fault, the velocity is initially several orders of magnitude smaller than the cutoff, but there is a region of size $0.75W$ in which the initial slip rate is $V_c/10$. In each simulation, an event begins in this high-velocity region and propagates across the fault. The fronts approach steadily propagating profiles after traveling a distance shorter than $2W$. We examine their properties after that steady propagation is reached.

E2. Predicting the Maximum Velocity Given the Initial Conditions

[130] To verify that our estimates of K_c and K_{mod} are accurate, we use them to predict the maximum velocities in a number of steadily propagating simulations. Since we specify the initial stress in these simulations, we know K_u, the uniform stress drop contribution to K. Since K_u must equal $|K_c + K_{\mathrm{mod}}|$ and we know the initial state, we can determine the maximum velocity required to obtain the predicted $K_c + K_{\mathrm{mod}}$. This is illustrated graphically in Figure 9. The horizontal dotted lines indicate the value of K_u for several different stress drops and W, and the intersection of these lines with the $|K_c + K_{\mathrm{mod}}|$ curves determines the predicted maximum velocity.

[131] We have run steadily propagating simulations with a range of initial stresses and states. In Figure E1, the colored numbers are the maximum velocities from a number of simulations with $\theta_i = 10^4 D_c/V_c$. Values of 0 indicate that the event failed to propagate across the fault. For comparison, the black numbers to the right of the colored numbers are the predicted $V_{\mathrm{max}}/V_{\tau\text{-min}}$. A value of zero here means that we predict that an event cannot propagate steadily with a maximum velocity larger than $V_{\tau\text{-min}}$. For further comparison, in the inset axes, we plot the observed and predicted maximum velocities.

[132] If we consider only simulations with $V_{\mathrm{max}}/V_{\tau\text{-min}} > 15$, most of the predicted velocities match the simulation results to within 10%, even as the maximum velocity varies by more than a factor of 10 among the simulations. Thus it appears that the predicted dependence of $K_c + K_{\mathrm{mod}}$ on V_{max} is consistent with the simulation results. There are some small discrepancies; the predicted velocities are about 15% smaller than the observed values at low slip rates and about 15% larger at high slip rates. Given the uncertainties in the fits to stress behind the front and the calculation of K_c, that small inaccuracy seems plausible, and we conclude that our modeled variation in $K_c + K_{\mathrm{mod}}$ with maximum velocity reasonably matches the simulation results.

E3. Minimum Stress Drop and Velocity for Propagation

[133] If the stress drop in an event is small, K_u is small, $K_c + K_{\mathrm{mod}}$ is small, and V_{max} is small. However, if the initial stress is too small, the event never achieves steady propagation. To investigate this minimum stress drop, we consider the minimum V_{max} that can exist in a steadily propagating front. One might argue that the smallest allowable V_{max} should be the minimum steady state stress velocity $V_{\tau\text{-min}}$. If V_{max} were smaller than $V_{\tau\text{-min}}$, any small perturbation would allow the fault to accelerate and evolve along the velocity-weakening section of the steady state curve to a lower stress.

[134] We can compute a predicted minimum stress drop based on the assumption that the minimum V_{max} is $V_{\tau\text{-min}}$. Indeed, in Figure E1, we plotted 0 in black when the stress drop was too small for the predicted V_{max} to be larger than $V_{\tau\text{-min}}$. This predicted minimum stress drop matches the simulation results to within $0.125b\sigma$. However, it is systematically smaller than the actual minimum, especially for a/b of 0.7 and 0.8. At least some of this discrepancy arises because stress recovers from its minimum value behind the front, and it recovers more when a/b and V_{max} are small. We do not account for this recovery when we estimate the contributions to K, so we overestimate $K_u + K_{\mathrm{mod}}$ and therefore V_{max}. *Hawthorne* [2012] has investigated the parameters that affect the stress recovery, but it is difficult to accurately predict its value. We do not attempt to modify K_u to account for it. Instead, we simply note that the stress drop required for propagation is approximately the stress drop required for V_{max} to be $15V_{\tau\text{-min}}$.

[135] In cycle simulations, the maximum velocity in large events is 10 to $40V_{\tau\text{-min}}$. These values are larger than the minimum velocity required for propagation, because in cycle simulations, events nucleate only at discrete intervals. Usually, they do not nucleate exactly at the time when K_u becomes large enough to obtain the minimum allowable V_{max}, as discussed in section 5.3.

[136] **Acknowledgments.** We thank two anonymous reviewers and the associate editor for comments on the manuscript. This research was supported by NSF grant EAR-0911378. J.C.H. was also supported by a Charlotte Elizabeth Procter Fellowship from Princeton University.

References

Ampuero, J.-P., and A. M. Rubin (2008), Earthquake nucleation on rate and state faults—Aging and slip laws, *J. Geophys. Res.*, *113*, B01302, doi:10.1029/2007JB005082.

Ariyoshi, K., T. Hori, J.-P. Ampuero, Y. Kaneda, T. Matsuzawa, R. Hino, and A. Hasegawa (2009), Influence of interaction between small asperities on various types of slow earthquakes in a 3-D simulation for a subduction plate boundary, *Gondwana Res.*, *16*(3-4), 534–544, doi:10.1016/j.gr.2009.03.006.

Audet, P., M. G. Bostock, N. I. Christensen, and S. M. Peacock (2009), Seismic evidence for overpressured subducted oceanic crust and megathrust fault sealing, *Nature*, *457*, 76–78, doi:10.1038/nature07650.

Bar Sinai, Y., E. A. Brener, and E. Bouchbinder (2012), Slow rupture of frictional interfaces, *Geophys. Res. Lett.*, *39*, L03308, doi:10.1029/2011GL050554.

Barenblatt, G. (1962), The mathematical theory of equilibrium cracks in brittle fracture, in *Advances in Applied Mechanics,* vol. 7, edited by Th. von Kármán, F. H. van den Dungen, G. Kuerti, and L. Howarth, pp. 55–129, Elsevier, New York and London.

Bartlow, N. M., S. Miyazaki, A. M. Bradley, and P. Segall (2011), Space-time correlation of slip and tremor during the 2009 cascadia slow slip event, *Geophys. Res. Lett.*, *38*, L18309, doi:10.1029/2011GL048714.

Bayart, E., A. M. Rubin, and C. Marone (2006), Evolution of fault friction following large velocity jumps, *Eos Trans. AGU*, pp. Fall Meet. Suppl., Abstract S31A–180.

Beeler, N. (2009), Constructing constitutive relationships for seismic and aseismic fault slip, *Pure Appl. Geophys.*, *166*(10), 1775–1798, doi:10.1007/s00024-009-0523-0.

Bizzarri, A., and M. Cocco (2003), Slip-weakening behavior during the propagation of dynamic ruptures obeying rate- and state-dependent friction laws, *J. Geophys. Res.*, *108*, 2373, doi:10.1029/2002JB002198.

Boettcher, M. S., G. Hirth, and B. Evans (2007), Olivine friction at the base of oceanic seismogenic zones, *J. Geophys. Res.*, *112*, B01205, doi:10.1029/2006JB004301.

Bouchon, M., H. Sekiguchi, K. Irikura, and T. Iwata (1998), Some characteristics of the stress field of the 1995 Hyogo-ken Nanbu (kobe) earthquake, *J. Geophys. Res.*, *103*, 24,271–24,282, doi:10.1029/98JB02136.

Boyarko, D. C., and M. R. Brudzinski (2010), Spatial and temporal patterns of nonvolcanic tremor along the southern Cascadia subduction zone, *J. Geophys. Res.*, *115*, B00A22, doi:10.1029/2008JB006064.

Brechet, Y., and Y. Estrin (1994), The effect of strain-rate sensitivity on dynamic friction of metals, *Scr. Metall. Mater.*, *30*(11), 1449–1454.

Brudzinski, M. R., and R. M. Allen (2007), Segmentation in episodic tremor and slip all along Cascadia, *Geology*, *35*(10), 907–910, doi:10.1130/G23740A.1.

Creager, K. C., A. J. Klaus, A. Wech, H. Houston, and J. E. Vidale (2011), Nucleation of northern Cascadia episodic tremor and slip events, *Eos Trans. AGU*, pp. Fall Meet. Suppl., Abstract S33C–01.

Dieterich, J. H. (1972), Time-dependent friction in rocks, *J. Geophys. Res.*, *77*(20), 3690–3697, doi:10.1029/JB077i020p03690.

Dieterich, J. H. (1992), Earthquake nucleation on faults with rate-dependent and state-dependent strength, *Tectonophysics*, *211*(1-4), 115–134, doi:10.1016/0040-1951(92)90055-B.

Dieterich, J. H. (2007), Applications of rate- and state-dependent friction to models of fault slip and earthquake occurrence, in *Treatise on Geophysics*, edited by Kanamori, H., and G. Schubert, Earthquake Seismology, vol. 4, Elsevier, Amsterdam, 6054.

Dragert, H., and K. Wang (2011), Temporal evolution of an episodic tremor and slip event along the northern Cascadia margin, *J. Geophys. Res.*, *116*, B12406, doi:10.1029/2011JB008609.

Dragert, H., K. L. Wang, and T. S. James (2001), A silent slip event on the deeper Cascadia subduction interface, *Science*, *292*(5521), 1525–1528, doi:10.1126/science.1060152.

Estrin, Y., and Y. Brechet (1996), On a model of frictional sliding, *Pure Appl. Geophys.*, *147*(4), 745–762, doi:10.1007/BF01089700.

Fletcher, J. B., and A. McGarr (2006), Distribution of stress drop, stiffness, and fracture energy over earthquake rupture zones, *J. Geophys. Res.*, *111*, B03312, doi:10.1029/2004JB003396.

Fukuda, J., K. M. Johnson, K. M. Larson, and S. Miyazaki (2009), Fault friction parameters inferred from the early stages of afterslip following the 2003 TokachiâĂŘoki earthquake, *J. Geophys. Res.*, *114*, B04412, doi:10.1029/2008JB006166.

Ghosh, A., J. E. Vidale, J. R. Sweet, K. C. Creager, A. G. Wech, and H. Houston (2010a), Tremor bands sweep cascadia, *Geophys. Res. Lett.*, *37*, L08301, doi:10.1029/2009GL042301.

Ghosh, A., J. E. Vidale, J. R. Sweet, K. C. Creager, A. G. Wech, H. Houston, and E. E. Brodsky (2010b), Rapid continuous streaking of tremor in Cascadia, *Geochem. Geophys. Geosyst.*, *11*, Q12010, doi:10.1029/2010GC003305.

Gomberg, J. (2010), Lessons from (triggered) tremor, *J. Geophys. Res.*, *115*, B10302, doi:10.1029/2009JB007011.

Guatteri, M., P. Spudich, and G. C. Beroza (2001), Inferring rate and state friction parameters from a rupture model of the 1995 Hyogo-ken Nanbu (kobe) Japan earthquake, *J. Geophys. Res.*, *106*(26), 511–526.

Hawthorne, J. C. (2012), Observations and modeling of temporal variability in slow slip events, Ph.D., Princeton University, New Jersey.

Hawthorne, J. C., and A. M. Rubin (2010), Tidal modulation of slow slip in Cascadia, *J. Geophys. Res.*, *115*, B09406, doi:10.1029/2010JB007502.

Hawthorne, J. C., and A. M. Rubin (2013), Tidal modulation and back-propagating fronts in slow slip events simulated with a velocity-weakening to velocity-strengthening friction law, *J. Geophys. Res. Solid Earth*, *118*(3), 1216–1239, doi:10.1002/jgrb.50107.

He, C., W. Yao, Z. Wang, and Y. Zhou (2006), Strength and stability of frictional sliding of gabbro gouge at elevated temperatures, *Tectonophysics*, *427*(1-4), 217–229, doi:10.1016/j.tecto.2006.05.023.

He, C., Z. Wang, and W. Yao (2007), Frictional sliding of gabbro gouge under hydrothermal conditions, *Tectonophysics*, *445*(3-4), 353–362, doi:10.1016/j.tecto.2007.09.008.

Hindmarsh, A. (1983), ODEPACK a systematized collection of ODE solvers, *IMACS Trans. Sci. Comput.*, *1*, 55–64.

Hirose, H., and K. Obara (2010), Recurrence behavior of short-term slow slip and correlated nonvolcanic tremor episodes in western Shikoku, southwest Japan, *J. Geophys. Res.*, *115*, B00A21, doi:10.1029/2008JB006050.

Houston, H., B. G. Delbridge, A. G. Wech, and K. C. Creager (2011), Rapid tremor reversals in Cascadia generated by a weakened plate interface, *Nat. Geosci.*, *4*(6), 404–409, doi:10.1038/ngeo1157.

Ida, Y. (1973), The maximum acceleration of seismic ground motion, *Bull. Seismol. Soc. Am.*, *63*(3), 959–968.

Ide, S. (2010), Striations duration migration and tidal response in deep tremor, *Nature*, *466*(7304), 356–359, doi:10.1038/nature09251.

Ide, S. (2012), Variety and spatial heterogeneity of tectonic tremor worldwide, *J. Geophys. Res.*, *117*, B03302, doi:10.1029/2011JB008840.

Ide, S., and M. Takeo (1997), Determination of constitutive relations of fault slip based on seismic wave analysis, *J. Geophys. Res.*, *102*, 27,379–27,392.

Kanu, C., and K. Johnson (2011), Arrest and recovery of frictional creep on the southern Hayward fault triggered by the 1989 Loma Prieta, California, earthquake and implications for future earthquakes, *J. Geophys. Res.*, *116*, B04403, doi:10.1029/2010JB007927.

Kao, H., S.-J. Shan, H. Dragert, G. Rogers, J. F. Cassidy, K. Wang, T. S. James, and K. Ramachandran (2006), Spatial-temporal patterns of seismic tremors in northern Cascadia, *J. Geophys. Res.*, *111*, B03309, doi:10.1029/2005JB003727.

Kilgore, B. D., M. L. Blanpied, and J. H. Dieterich (1993), Velocity dependent friction of granite over a wide range of conditions, *Geophys. Res. Lett.*, *20*(10), 903–906.

Kodaira, S., T. Iidaka, A. Kato, J.-O. Park, T. Iwasaki, and Y. Kaneda (2004), High pore fluid pressure may cause silent slip in the Nankai Trough, *Science*, *304*(5675), 1295–1298, doi:10.1126/science.1096535.

Lambert, A., H. Kao, G. Rogers, and N. Courtier (2009), Correlation of tremor activity with tidal stress in the northern Cascadia subduction zone, *J. Geophys. Res.*, *114*, B00A08, doi:10.1029/2008JB006038.

Lawn, B. (1993), *Fracture of Brittle Solids* (2nd edn), Cambridge University Press, Cambridge, UK.

Liu, Y., and J. R. Rice (2009), Slow slip predictions based on granite and gabbro friction data compared to GPS measurements in northern Cascadia, *J. Geophys. Res.*, *114*, B09407, doi:10.1029/2008JB006142.

Liu, Y., and A. M. Rubin (2010), Role of fault gouge dilatancy on aseismic deformation transients, *J. Geophys. Res.*, *115*, B10414, doi:10.1029/2010JB007522.

Liu, Y. J., and J. R. Rice (2005), Aseismic slip transients emerge spontaneously in three-dimensional rate and state modeling of subduction earthquake sequences, *J. Geophys. Res.*, *110*, B08307, doi:10.1029/2004JB003424.

Liu, Y. J., and J. R. Rice (2007), Spontaneous and triggered aseismic deformation transients in a subduction fault model, *J. Geophys. Res.*, *112*, B09404, doi:10.1029/2007JB004930.

Marone, C. (1998), *Annu. Rev. Earth Planet. Sci.*, *26*, 643–696, doi:10.1146/annurev.earth.26.1.643.

Matsubara, M., K. Obara, and K. Kasahara (2009), High-VP/VS zone accompanying non-volcanic tremors and slow-slip events beneath southwestern Japan, *Tectonophysics*, *472*(14), 6–17, doi:10.1016/j.tecto.2008.06.013.

Matsuzawa, T., H. Hirose, B. Shibazaki, and K. Obara (2010), Modeling short- and long-term slow slip events in the seismic cycles of large subduction earthquakes, *J. Geophys. Res.*, *115*, B12301, doi:10.1029/2010JB007566.

Mitsui, Y., and K. Hirahara (2008), Long-term slow slip events are not necessarily caused by high pore fluid pressure at the plate interface: An implication from two-dimensional model calculations, *Geophys. J. Int.*, *174*(1), 331–335, doi:10.1111/j.1365-246X.2008.03832.x.

Moore, D. E., D. A. Lockner, M. Shengli, R. Summers, and J. D. Byerlee (1997), Strengths of serpentinite gouges at elevated temperatures, *J. Geophys. Res.*, *102*, 14,787–14,802.

Nakatani, M., and C. H. Scholz (2006), Intrinsic and apparent short-time limits for fault healing: Theory, observations, and implications for velocity-dependent friction, *J. Geophys. Res.*, *111*, B12208, doi:10.1029/2005JB004096.

Obara, K. (2002), Nonvolcanic deep tremor associated with subduction in southwest Japan, *Science*, *296*(5573), 1679–1681, doi:10.1126/science.1070378.

Obara, K. (2010), Phenomenology of deep slow earthquake family in southwest Japan: Spatiotemporal characteristics and segmentation, *J. Geophys. Res.*, *115*, B00A25, doi:10.1029/2008JB006048.

Obara, K., H. Hirose, F. Yamamizu, and K. Kasahara (2004), Episodic slow slip events accompanied by non-volcanic tremors in southwest Japan subduction zone, *Geophys. Res. Lett.*, *31*, L23602, doi:10.1029/2004GL020848.

Okubo, P. G., and J. H. Dietrich (1986), State variable fault constitutive relations for dynamic slip, in *Earthquake Source Mechanics, Geophysical Monographs*, edited by Das, S., J. Boatwright, and C. H. Scholz, vol. 6, American Geophysical Union, Washington D.C, 25–35.

Peacock, S. M., N. I. Christensen, M. G. Bostock, and P. Audet (2011), High pore pressures and porosity at 35 km depth in the Cascadia subduction zone, *Geology*, *39*(5), 471–474, doi:10.1130/G31649.1.

Peng, Z., and J. Gomberg (2010), An integrated perspective of the continuum between earthquakes and slow-slip phenomena, *Nat. Geosci.*, *3*(9), 599–607, doi:10.1038/ngeo940.

Perfettini, H., and J. P. Ampuero (2008), Dynamics of a velocity strengthening fault region: Implications for slow earthquakes and postseismic slip, *J. Geophys. Res.-Solid Earth*, *113*, B09411, doi:10.1029/2007JB005398.

Reinen, L. A., J. D. Weeks, and T. E. Tullis (1994), The frictional behavior of lizardite and antigorite serpentinites: Experiments, constitutive models, and implications for natural faults, *Pure Appl. Geophys.*, *143*(1-3), 317–358, doi:10.1007/BF00874334.

Rice, J. R. (1980), The mechanics of earthquake rupture, in *Physics of the Earth's Interior (Proc. Intl. School of Physics, "E. Fermi" Course 78)*, edited by Dziewonski, A. M., and E. Boschi, pp. 555–650, Italian Physical Society / North Holland Publishing Co., Amsterdam, The Netherlands.

Rice, J. R., N. Lapusta, and K. Ranjith (2001), Rate and state dependent friction and the stability of sliding between elastically deformable solids, *J. Mech. Phys. Solids*, *49*(9), 1865–1898, doi:10.1016/S0022-5096(01)00042-4.

Rubin, A. M. (2008), Episodic slow slip events and rate-and-state friction, *J. Geophys. Res.*, *113*, B11414, doi:10.1029/2008JB005642.

Rubin, A. M., and J. P. Ampuero (2005), Earthquake nucleation on (aging) rate and state faults, *J. Geophys. Res.*, *110*, B11312, doi:10.1029/2005JB003686.

Rubinstein, J. L., J. E. Vidale, J. Gomberg, P. Bodin, K. C. Creager, and S. D. Malone (2007), Non-volcanic tremor driven by large transient shear stresses, *Nature*, *448*(7153), 579–582, doi:10.1038/nature06017.

Rubinstein, J. L., M. La Rocca, J. E. Vidale, K. C. Creager, and A. G. Wech (2008), Tidal modulation of nonvolcanic tremor, *Science*, *319*(5860), 186–189, doi:10.1126/science.1150558.

Rubinstein, J. L., J. Gomberg, J. E. Vidale, A. G. Wech, H. Kao, K. C. Creager, and G. Rogers (2009), Seismic wave triggering of nonvolcanic tremor, episodic tremor and slip, and earthquakes on Vancouver island, *J. Geophys. Res.*, *114*, B00A01, doi:10.1029/2008JB005875.

Ruina, A. (1983), Slip instability and state variable friction laws, *J. Geophys. Res.*, *88*(B12), 10,359–10,370, doi:10.1029/JB088iB12p10359.

Ruina, A. L. (1980), Friction laws and instabilities: A quasistatic analysis of some dry frictional behaviors, Ph.D., Brown University, Providence, RI.

Schmidt, D. A., and H. Gao (2010), Source parameters and time-dependent slip distributions of slow slip events on the Cascadia subduction zone from 1998 to 2008, *J. Geophys. Res.*, *115*, B00A18, doi:10.1029/2008JB006045.

Schwartz, S. Y., and J. M. Rokosky (2007), Slow slip events and seismic tremor at circum-Pacific subduction zones, *Rev. Geophys.*, *45*, RG3004, doi:10.1029/2006RG000208.

Segall, P., and J. R. Rice (1995), Dilatancy compaction and slip instability of a fluid-infiltrated fault, *J. Geophys. Res.*, *100*(B11), 22,155–22,171, doi:10.1029/95JB02403.

Segall, P., A. M. Rubin, A. M. Bradley, and J. R. Rice (2010), Dilatant strengthening as a mechanism for slow slip events, *J. Geophys. Res.*, *115*, B12305, doi:10.1029/2010JB007449.

Sekine, S., H. Hirose, and K. Obara (2010), Along-strike variations in short-term slow slip events in the southwest Japan subduction zone, *J. Geophys. Res.*, *115*, B00A27, doi:10.1029/2008JB006059.

Shibazaki, B., and Y. Iio (2003), On the physical mechanism of silent slip events along the deeper part of the seismogenic zone, *Geophys. Res. Lett.*, *30*(9), 4, doi:10.1029/2003GL017047.

Shibazaki, B., and T. Shimamoto (2007), Modelling of short-interval silent slip events in deeper subduction interfaces considering the frictional properties at the unstable-stable transition regime, *Geophys. J. Int.*, *171*(1), 191–205, doi:10.1111/j.1365-246X.2007.03434.x.

Shibazaki, B., S. Bu, T. Matsuzawa, and H. Hirose (2010), Modeling the activity of short-term slow slip events along deep subduction interfaces beneath Shikoku, southwest Japan, *J. Geophys. Res.*, *115*, B00A19, doi:10.1029/2008JB006057.

Shibazaki, B., K. Obara, T. Matsuzawa, and H. Hirose (2012), Modeling of slow slip events along the deep subduction zone in the Kii Peninsula and Tokai regions, southwest Japan, *J. Geophys. Res.*, *117*, B06311, doi:10.1029/2011JB009083.

Shimamoto, T. (1986), Transition between frictional slip and ductile flow for halite shear zones at room temperature, *Science*, *231*(4739), 711–714, doi:10.1126/science.231.4739.711.

Skarbek, R. M., A. W. Rempel, and D. A. Schmidt (2012), Geologic heterogeneity can produce aseismic slip transients, *Geophys. Res. Lett.*, *39*, L21306, doi:10.1029/2012GL053762.

Suzuki, T., and T. Yamashita (2009), Dynamic modeling of slow earthquakes based on thermoporoelastic effects and inelastic generation of pores, *J. Geophys. Res.*, *114*, B00A04, doi:10.1029/2008JB006042.

Szeliga, W., T. Melbourne, M. Santillan, and M. Miller (2008), GPS constraints on 34 slow slip events within the Cascadia subduction zone, 1997–2005, *J. Geophys. Res.*, *113*, B04404, doi:10.1029/2007JB004948.

Tada, H., P. C. Paris, and G. R. Irwin (2000), *The Stress Analysis of Cracks Handbook* (3rd edn), The American Society of Engineers, New York.

Wang, K., H. Dragert, H. Kao, and E. Roeloffs (2008), Characterizing an "uncharacteristic" ETS event in northern Cascadia, *Geophys. Res. Lett.*, *35*, L15303, doi:10.1029/2008GL034415.

Wech, A. G., and K. C. Creager (2008), Automated detection and location of Cascadia tremor, *Geophys. Res. Lett.*, *35*, L20302, doi:10.1029/2008GL035458.

Wech, A. G., and K. C. Creager (2011), A continuum of stress, strength and slip in the Cascadia subduction zone, *Nat. Geosci.*, *4*(9), 624–628, doi:10.1038/ngeo1215.

Wech, A. G., K. C. Creager, and T. I. Melbourne (2009), Seismic and geodetic constraints on Cascadia slow slip, *J. Geophys. Res.*, *114*, B10316, doi:10.1029/2008JB006090.

Wech, A. G., K. C. Creager, H. Houston, and J. E. Vidale (2010), An earthquake-like magnitude-frequency distribution of slow slip in northern Cascadia, *Geophys. Res. Lett.*, *37*, L22310, doi:10.1029/2010GL044881.

Weeks, J. D. (1993), Constitutive laws for high-velocity frictional sliding and their influence on stress drop during unstable slip, *J. Geophys. Res.*, *98*(B10), 17,637–17,648, doi:10.1029/93JB00356.

Yamashita, T., and T. Suzuki (2011), Dynamic modeling of slow slip coupled with tremor, *J. Geophys. Res.*, *116*, B05301, doi:10.1029/2010JB008136.

Yoshida, S., and N. Kato (2003), Episodic aseismic slip in a two-degree-of-freedom block-spring model, *Geophys. Res. Lett.*, *30*(13), 1681, doi:10.1029/2003GL017439.